

Piezoelectricity and Topological Quantum Phase Transitions in Two-Dimensional Spin-Orbit Coupled Crystals with Time-Reversal Symmetry

Jiabin Yu¹ and Chao-Xing Liu^{1,*}

¹*Department of Physics, the Pennsylvania State University, University Park, PA, 16802*

Finding new physical responses that signal topological quantum phase transitions is of both theoretical and experimental importance. Here, we demonstrate that the piezoelectric response can change discontinuously across a topological quantum phase transition in two-dimensional time-reversal invariant systems with spin-orbit coupling, thus serving as a direct probe of the transition. We study all gap closing cases for all 7 plane groups that allow non-vanishing piezoelectricity and find that any gap closing with 1 fine-tuning parameter between two gapped states changes either the Z_2 invariant or the locally stable valley Chern number. The jump of the piezoelectric response is found to exist for all these transitions, and we propose the HgTe/CdTe quantum well and BaMnSb₂ as two potential experimental platforms. Our work provides a general theoretical framework to classify topological quantum phase transitions and reveals their ubiquitous relation to the piezoelectric response.

CONTENTS

I. Introduction	2
II. Results	3
A. PET jump across a Direct QSH-NI TQPT	3
B. Classification of Direct 2D TQPTs and PET jumps for 7 PGs	5
C. HgTe/CdTe Quantum Well	7
D. Layered Material BaMnSb ₂	7
III. Discussion	8
IV. Methods	10
A. Expression for the PET	10
B. PG $p1$	10
C. PGs $p1m1$, $c1m1$, and $p1g1$	10
D. PG $p3$	11
E. PGs $p31m$ and $p3m1$	11
F. Valley CN	11
V. Acknowledgement	12
A. Derivation of the PET	12
B. Details on PET for Each PG	13
1. PG $p1$	13
2. PGs $p1m1$, $c1m1$ and $p1g1$	13
a. Scenario (i): TRIM	14
b. Scenario (ii): $\mathcal{U} \in \mathcal{G}_0$ but $\mathcal{T} \notin \mathcal{G}_0$	14
c. Scenario (iii): $\mathcal{UT} \in \mathcal{G}_0$ but $\mathcal{T} \notin \mathcal{G}_0$	15
d. Scenario (iv): trivial \mathcal{G}_0	15
3. PG $p3$	16
a. Scenario (i): TRIM	16
b. Scenario (ii): $C_3 \in \mathcal{G}_0$ and $\mathcal{T} \notin \mathcal{G}_0$	18
c. Scenario (iii): trivial \mathcal{G}_0	19
4. PG $p31m$ and PG $p3m1$	19

* cx156@psu.edu

a. Scenario (i): TRIM	19
b. Scenario (ii): $\mathcal{U} \in \mathcal{G}_0$ and $\mathcal{T} \notin \mathcal{G}_0$	20
c. Scenario (iii): $\mathcal{UT} \in \mathcal{G}_0$ and $\mathcal{T} \notin \mathcal{G}_0$	20
d. Scenario (iv): trivial \mathcal{G}_0	21
5. 10 PGs with 2D Inversion or C_2	21
C. Numbers of FTPs and Effective Models for the Gap Closing	22
1. PG $p1$	22
a. Not TRIM	22
b. TRIM	22
2. $p1m1$, $c1m1$, and $p1g1$	23
a. Scenario (i): TRIM	23
b. Scenario (ii): $\mathcal{U} \in \mathcal{G}_0$ but $\mathcal{T} \notin \mathcal{G}_0$	23
c. Scenario (iii): $\mathcal{UT} \in \mathcal{G}_0$ but $\mathcal{T} \notin \mathcal{G}_0$	23
3. $p3$	23
a. Scenario (i): TRIM	23
b. Scenario (ii): $C_3 \in \mathcal{G}_0$ and $\mathcal{T} \notin \mathcal{G}_0$	24
4. $p31m$ and $p3m1$	24
a. Scenario (i): TRIM	24
b. Scenario (iii): $\mathcal{UT} \in \mathcal{G}_0$ and $\mathcal{T} \notin \mathcal{G}_0$	24
D. VCN in Tight-Binding Model	25
E. (111) HgTe/CdTe Quantum Well	26
1. d -induced PET jump for $\mathcal{E} = 0$	26
2. \mathcal{E} -induced PET jump for fixed d	27
3. Projection of the Kane Model	27
4. Construction of the Hamiltonian based on symmetry	28
F. BaMnSb ₂	29
1. Review	30
2. TB Calculation of PET	31
3. Effective Model Analysis	31
References	32

I. INTRODUCTION

The discovery of topological phases and topological phase transitions has revolutionized our understanding of quantum states of matter and quantum phase transitions (1–3). Two topologically distinct gapped phases cannot be adiabatically connected; if the system continuously evolves from one phase to the other, a topological quantum phase transition (TQPT) with the energy gap closing (GC) must occur. A direct way to probe such TQPTs is to detect the discontinuous change of certain physical response functions. Celebrated examples include the jump of the Hall conductance across the plateau transition in the integer quantum Hall system (4, 5), the jump of the two-terminal conductance across the TQPT between the quantum spin Hall (QSH) state and normal insulator (NI) state in a two-dimensional (2D) time-reversal (TR) invariant system (6), and the jump of the magnetoelectric coefficient across the TQPT between the strong topological insulator phase and NI phase in a 3D TR invariant system (7–10). The physical responses in all these examples are induced by the electromagnetic field. A natural question then arises: can we detect TQPTs with other types of perturbation?

Here we theoretically answer this question in the affirmative: the discontinuous change of the piezoelectric response is a ubiquitous and direct signature of 2D TQPTs. The piezoelectric effect, the electric charge response induced by the applied strain, is characterized by the piezoelectric tensor (PET) to the leading order. PET was originally defined to relate the change of the charge polarization \mathbf{P} with the infinitesimal homogeneous strain, which reads (11)

$$\gamma_{ijk} = \left. \frac{\partial P_i}{\partial u_{jk}} \right|_{u_{jk} \rightarrow 0}, \quad (1)$$

where $u_{ij} = (\partial_{x_i} u_j + \partial_{x_j} u_i)/2$ is the strain tensor and \mathbf{u} is the displacement at \mathbf{x} . The modern theory of polarization (12–14) later identified the above definition as improper (15) due to the ambiguity of \mathbf{P} in crystals, while the proper definition adds the adiabatic time dependence to u_{jk} and relates it to the bulk current density J_i that can change the surface charge:

$$\gamma_{ijk} = \left. \frac{\partial J_i}{\partial \dot{u}_{jk}} \right|_{u_{jk}, \dot{u}_{jk} \rightarrow 0}. \quad (2)$$

With Eq. (2), the PET of an insulating crystal has been derived as (15, 16)

$$\gamma_{ijk} = -e \int \frac{d^2 k}{(2\pi)^2} \sum_n F_{k_i, u_{jk}}^n \Big|_{u_{jk} \rightarrow 0}, \quad (3)$$

where the integral is over the entire first Brillouin zone (1BZ), and n ranges over all occupied bands. The $F_{k_i, u_{jk}}^n$ term has a Berry-curvature-like expression

$$F_{k_i, u_{jk}}^n = (-i) [\langle \partial_{k_i} \varphi_{n, \mathbf{k}} | \partial_{u_{jk}} \varphi_{n, \mathbf{k}} \rangle - (k_i \leftrightarrow u_{jk})] \quad (4)$$

with $|\varphi_{n, \mathbf{k}}\rangle$ the periodic part of the Bloch state in the presence of the strain. (See the Methods for more details.) The expression indicates an extreme similarity between Eq. (3) and the expression for the Chern number (CN) (5). It is this similarity that motivates us to study the relation between the PET and the TQPT.

Despite the similarity, the topology connected to the PET is essentially different from the CN, since the PET can exist in TR invariant systems whose CNs always vanish. We, in this work, study the piezoelectric response of 2D TR invariant systems in the presence of the significant spin-orbit coupling (SOC) and demonstrate the jump of all symmetry-allowed PET components across the TQPT. In particular, we focus on the 7 out of the 17 plane groups (PGs) that allow non-vanishing PET components (17, 18), including $p1$, $p1m1$, $c1m1$, $p1g1$, $p3$, $p3m1$, and $p31m$. The two-fold rotation C_2 (with the axis perpendicular to the 2D plane) or the 2D inversion restricts the PET to zero in the other 10 PGs (19), according to $\gamma_{ijk} = \sum_{i'j'k'} R_{ii'} R_{jj'} R_{kk'} \gamma_{i'j'k'}$ for any $O(2)$ symmetry R of the 2D material. Through a systematic study, we find that any GC between two gapped states that only requires 1 fine-tuning parameter is a TQPT in the sense that it changes either the Z_2 index (1, 2) or the valley CN (20). Although the change of the valley CN is locally stable (21), we still treat the corresponding GC as a TQPT, since the two states cannot be adiabatically connected when the valley is well defined. All the TQPTs contain no stable gapless phase in between two gapped phases, and thereby we refer to them as the *direct* TQPTs. All PET components that are allowed by the crystalline symmetry exhibit discontinuous changes across any of the direct TQPTs, showing the ubiquitous connection. Interestingly, when the gap closes at momenta that are not TR invariant, the strain tensor u_{ij} acts as a pseudo-gauge field (22) at the TQPT, making the PET jump directly proportional to the change of the Z_2 index or the valley CN.

Our work presents a general framework for the PET jump across the TQPT in 2D TR invariant systems with SOC. The relation between the PET and the valley CN in the low-energy effective model has been studied in graphene with a staggered potential (23), h-BN (24, 25), and monolayer transition metal dichalcogenides (TMDs) XY_2 for $X=\text{Mo}/\text{W}$ and $Y=\text{S}/\text{Se}$ (25). However, these early works have *not* pointed out that it is the PET jump (well described within the low-energy effective model) that is the experimental signature directly related to the TQPT, while the PET itself at fixed parameters might contain the non-topological background given by high-energy bands. Moreover, these works, unlike our systematic study, only considered one specific plane group ($p3m1$) around one specific type of momenta (K, K'). The relation between the PET and the Z_2 index were not explored either. Besides, graphene and h-BN have neglectable SOC, and the TMDs have a large gap, making them not suitable for realizing TQPT. We thereby propose two realistic material systems, the HgTe/CdTe quantum well (QW) and the layered material BaMnSb₂, as potential experimental platforms. The Z_2 TQPT and PET jump can be achieved by varying the thickness or the gate voltages in the HgTe/CdTe QW or by tuning lattice distortion in BaMnSb₂.

II. RESULTS

A. PET jump across a Direct QSH-NI TQPT

We start from a simple example of the TQPT discussed in Ref. (26). They (in the example of our interest) considered the case with no crystalline symmetries other than the lattice translation (PG $p1$) and focused on the GC at two

momenta $\pm \mathbf{k}_0$ that are not TR invariant momenta (TRIM), as labeled by red crosses in Fig. 1(a). The low-energy effective theory for the electron around \mathbf{k}_0 can be described by the Hamiltonian of a 2D massive Dirac fermion (26)

$$h_{+,0}(\mathbf{q}) = E_0(\mathbf{q})\sigma_0 + v_x q_1 \sigma_x + v_y q_2 \sigma_y + m\sigma_z, \quad (5)$$

where $\mathbf{q} = \mathbf{k} - \mathbf{k}_0$, m is the tuning parameter for the TQPT, and σ 's are Pauli matrices. In the above Hamiltonian, the unitary transformation on the bases and the scaling/rotation of \mathbf{q} are performed for the simplicity of the Hamiltonian; the latter generally makes q_1, q_2 along two non-orthogonal directions. (See Appendix C for details.) The effective Hamiltonian at $-\mathbf{k}_0$ is related to $h_{+,0}$ by the TR symmetry. After choosing appropriate bases at $-\mathbf{k}_0$, the TR symmetry can be represented as $\mathcal{T} = i\sigma_y \mathcal{K}$ with \mathcal{K} the complex conjugate, leading to

$$h_{-,0}(\mathbf{q}) = E_0(-\mathbf{q})\sigma_0 + v_x q_1 \sigma_x + v_y q_2 \sigma_y - m\sigma_z. \quad (6)$$

According to Ref. (26), the TQPT between the QSH insulator and the NI (distinguished by the Z_2 index) occurs when the mass m in $h_{\pm,0}(\mathbf{q})$ changes its sign. The argument used to determine change of the Z_2 index was presented in Ref. (27) and is discussed below for integrity. Since there is no inversion symmetry in PG $p1$, the Z_2 index can be determined from the CN of the contracted half first Brillouin zone (1BZ), where the half 1BZ is chosen such that its Kramers' partner covers the other half. Specifically, the Z_2 index is changed (unchanged) by the GC if the CN of the contracted half 1BZ changes by an odd (even) integer. Without loss of generality, let us choose the half 1BZ to contain \mathbf{k}_0 , as shown in Fig. 1(a). Since $h_{+,0}$ is a 2D gapped Dirac Hamiltonian, the CN of the contracted half 1BZ changes by $\Delta N_+ = -\text{sgn}(v_x v_y)$ as m increases from 0^- to 0^+ , featuring a direct QSH-NI TQPT as $v_x v_y$ is typically nonzero.

We next discuss the piezoelectric effect in this simple effective model. To do so, we need to introduce the electron-strain coupling around $\pm \mathbf{k}_0$ based on the TR symmetry:

$$h_{\pm,1}(u) = \xi_{0,ij}\sigma_0 u_{ij} \pm \xi_{a',ij}\sigma_{a'} u_{ij}, \quad (7)$$

where the duplicated indexes, including $a' = x, y, z$ and $i, j = 1, 2$, are summed over henceforth unless specified otherwise. ξ 's are the material-dependent coupling constants between the low-energy electrons and the strain tensor, which obey $\xi_{a,ij} = \xi_{a,ji}$ with $a = 0, x, y, z$ owing to $u_{ij} = u_{ji}$ and are related to the electron-phonon coupling (28). The full form of the effective Hamiltonian is then given by

$$h_{\pm}(\mathbf{q}, u) = h_{\pm,0}(\mathbf{q}) + h_{\pm,1}(u). \quad (8)$$

To use Eq. (3), we simplify Eq. (8) by neglecting the E_0 term, which has no influence on the piezoelectric response of insulators (see Appendix A). When $\xi_{x,ij} = \xi_{y,ij} = 0$, the Hamiltonian h_{\pm} has effective inversion symmetry within each valley, $\sigma_z h_{\pm}(-\mathbf{q}, u)\sigma_z = h_{\pm}(\mathbf{q}, u)$, which forbids the piezoelectric effect. Thus, $\xi_{0,ij}$ and $\xi_{z,ij}$ terms cannot contribute to the PET, and neglecting them leads to a further simplified version of Eq. (8):

$$h_{\pm}(\mathbf{q}, u) = [v_x(q_1 \pm A_1^{pse})]\sigma_x + [v_y(q_2 \pm A_2^{pse})]\sigma_y \pm m\sigma_z, \quad (9)$$

where $A_1^{pse} = \xi_{x,ij}u_{ij}/v_x$ and $A_2^{pse} = \xi_{y,ij}u_{ij}/v_y$. The above form suggests that the remaining strain terms, $\xi_{x,ij}$ and $\xi_{y,ij}$, serve as the pseudo-gauge field A_i^{pse} that has opposite signs for two valleys $\pm \mathbf{k}_0$ (10, 22, 25, 29). As the strain tensor only exists in the form of $q_i \pm A_i^{pse}$, the derivative with respect to u_{ij} in Eq. (3) can be replaced by the derivative with respect to the momentum as

$$\partial_{u_{ij}}|\varphi_{\pm, \mathbf{q}}\rangle = \frac{\partial A_{i'}^{pse}}{\partial u_{ij}} \partial_{A_{i'}^{pse}}|\varphi_{\pm, \mathbf{q}}\rangle = \pm \frac{\partial A_{i'}^{pse}}{\partial u_{ij}} \partial_{q_{i'}}|\varphi_{\pm, \mathbf{q}}\rangle, \quad (10)$$

where φ_{\pm} are the occupied bands of h_{\pm} . Substituting the above equation into Eq. (3) leads to

$$\begin{aligned} \gamma_{1ij}^{eff} &= -e \int \frac{d^2 q}{(2\pi)^2} \sum_{\alpha=\pm} \alpha F_{12}^{\alpha}(\mathbf{q}) \frac{\partial A_2^{pse}}{\partial u_{ij}} \\ \gamma_{2ij}^{eff} &= e \int \frac{d^2 q}{(2\pi)^2} \sum_{\alpha=\pm} \alpha F_{12}^{\alpha}(\mathbf{q}) \frac{\partial A_1^{pse}}{\partial u_{ij}}, \end{aligned} \quad (11)$$

where $F_{12}^{\pm}(\mathbf{q})$ is the conventional Berry curvature of the occupied band of $h_{\pm}(\mathbf{q}, 0)$. The superscript *eff* means that we neglect the contribution from bands beyond the effective model Eq. (8), indicating that the above equation is not

the complete PET. Nevertheless, it can accurately give the PET change across the TQPT since high-energy bands experience an adiabatic deformation and the corresponding background PET contribution should remain unchanged at the transition ($m = 0$). As m varies from 0^- to 0^+ , Eq. (11) gives the change of PET $\Delta\gamma_{ijk}$ as

$$\begin{aligned}\Delta\gamma_{1ij} &= -e \frac{\Delta N_+}{\pi} \frac{\xi_{y,ij}}{v_y} \\ \Delta\gamma_{2ij} &= e \frac{\Delta N_+}{\pi} \frac{\xi_{x,ij}}{v_x}.\end{aligned}\quad (12)$$

The PET jump shown in the above equation is nonzero since $v_x v_y$ and the electron-strain coupling ξ 's are typically non-zero. We thus conclude that for $p1$ group, a jump of PET that is directly proportional to the change of the Z_2 index occurs across the TQPT, when the gap closes not at TRIM.

The PET jump can be physically understood based on Eq. (2). Let first focus on one GC momentum, say \mathbf{k}_0 . Since the strain tensor couples to the electron in the way similar to the $U(1)$ gauge field as shown in Eq. (8), \dot{u}_{jk} should act like a electric field on the electron. According to Eq. (2), γ_{ijk} should then behave like the Hall conductance, whose jump is proportional to the change of CN ΔN_+ . Now we include the other GC momentum $-\mathbf{k}_0$. Unlike the actual $U(1)$ gauge field, the pseudo-gauge field given by the strain couples oppositely to the electron at the two GC momenta (Eq. (8)). The opposite signs of the coupling can cancel the opposite signs of the Berry curvature, and thus, in contrast to the actual Hall conductance, the contributions to γ_{ijk} from $\pm\mathbf{k}_0$ add up to a nonzero value instead of canceling each other, leading to the non-zero topological jump in Eq. (B2).

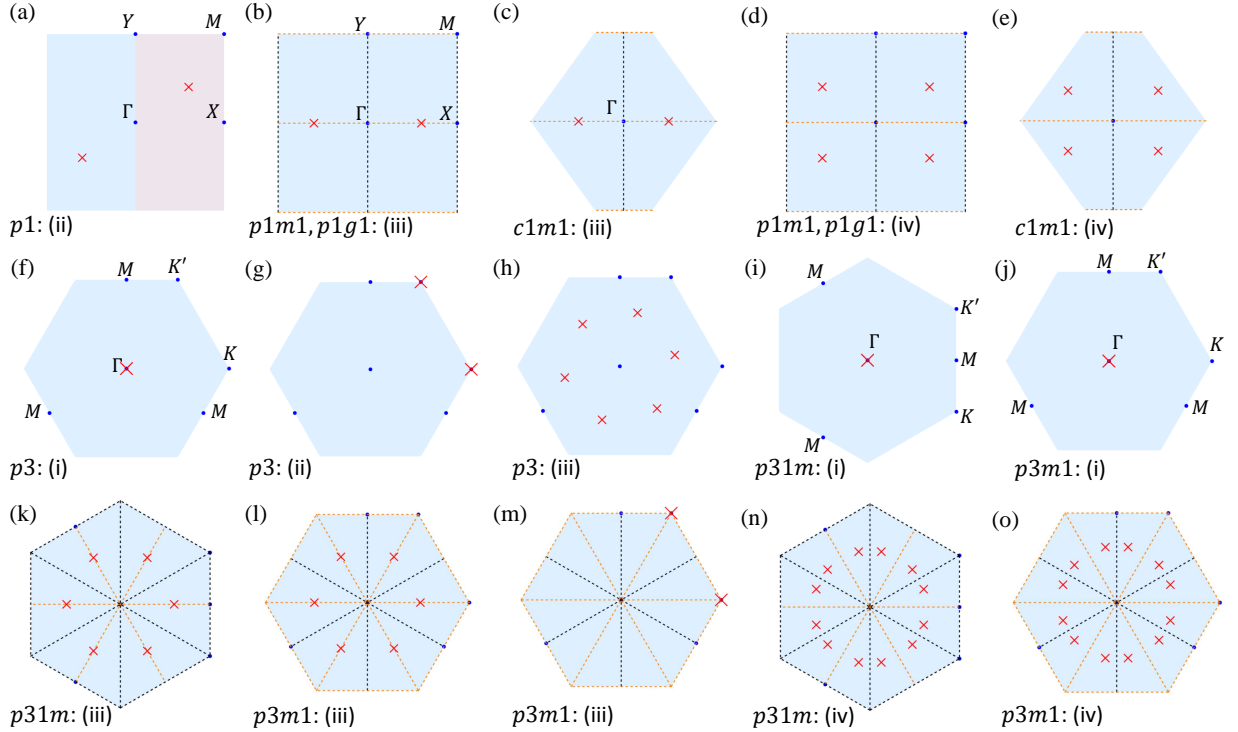


Fig 1: GC cases with 1 fine-tuning parameter. The figure shows the GC cases between insulating states with 1 fine-tuning parameter for all 7 PGs with non-vanishing PET. The red cross labels the GC momenta, the light blue background indicates the 1BZ, and the light red part in (a) indicates the half 1BZ. The black and orange dashed lines label the momenta invariant under the mirror/glide symmetry and the combination of mirror/glide and TR symmetries, respectively. The figures are first grouped according to the PGs and then ordered based on the GC scenarios listed in Tab. 1, whose labels are next to the names of the PGs.

B. Classification of Direct 2D TQPTs and PET jumps for 7 PGs

The above section discusses an example of 2D QSH-NI TQPT for the $p1$ PG and illustrates the main picture of the relation between the 2D TQPT and the PET jump. It is well-known that the crystalline symmetry imposes strong

constraints on the PET (19) (see the Methods). Topological states in different space/plane groups have been classified based on the topological quantum chemistry (30–36), the symmetry indicator (37–40), and other early methods (41–43). On the contrary, only a small number of works (26, 38, 44, 45) have studied the crystal symmetry constraint on the GC forms of the TQPTs. While the GC between non-degenerate states was studied in Ref. (45) for various layer groups in the presence of TR symmetry and SOC, the GC that involves degenerate states, like between two Kramers’ pairs, has not been explored. In particular, the topology change and the PET jump across any GC case with codimension 1 have not been discussed. As the substrate, on which the 2D materials are grown, typically reduces layer groups to PGs by breaking the extra symmetries, a study based on PG is typically enough for experimental predictions. Therefore, we next present a comprehensive study on the GC forms of TQPTs in all 7 PGs that allow nonvanishing PET, namely $p1$, $p1m1$, $c1m1$, $p1g1$, $p3$, $p31m$, and $p3m1$. The main results are summarized in Fig. 1 and Tab. 1, as discussed below. The other 10 PGs ($p2$, $p2mm$, $p2mg$, $p2gg$, $c2mm$, $p4$, $p4mm$, $p4gm$, $p6$, and $p6mm$) have vanishing PET due to the existence of inversion symmetry or C_2 rotation symmetry, and are briefly discussed in Appendix B.

TQPTs in different PGs can be analyzed in the following three steps. In the first step, we classify the GC based on the GC momenta and the symmetry property of the bands involved in the GC. To do so, we define the group \mathcal{G}_0 for a GC momentum \mathbf{k}_0 such that \mathcal{G}_0 contains all symmetry operations that leave \mathbf{k}_0 invariant (including the little group of \mathbf{k}_0 and TR-related operations). We start with a coarse classification based on \mathcal{G}_0 , which leads to 2 scenarios for $p1$, 3 scenarios for $p3$, and 4 scenarios for $p1m1$, $c1m1$, $p1g1$, $p31m$, and $p3m1$, as listed in Tab. 1 and the Methods. To illustrate this classification, we consider the $p3$ group as an example, which contains 3 different scenarios. In scenario (i), the GC is located at TRIM ($\mathcal{T} \in \mathcal{G}_0$), *i.e.* the Γ point or three M points in Fig. 1(f). In scenario (ii), the GC occurs simultaneously at K and K' where \mathcal{G}_0 contains C_3 but no \mathcal{T} (Fig. 1(g)). In scenario (iii), the GC occurs at six generic momenta (\mathcal{G}_0 only contains lattice translations) that are related by C_3 rotation and TR (Fig. 1(h)). The classification of GC momenta is coarse here since \mathcal{G}_0 can still vary within one scenario. For example, in scenario (i) of $p3$, \mathcal{G}_0 at Γ contains C_3 while \mathcal{G}_0 at M does not. Moreover, even at a certain GC momentum with a certain \mathcal{G}_0 , the symmetry properties of bands involved in the GC may vary. For example, at K in scenario (ii) of $p3$, the gap may close between two states with the same or different C_3 eigenvalues. Therefore, we further refine our classification by taking these subtleties into consideration and classify each GC scenario into finer GC cases.

In the second step, for each GC case, we construct a symmetry-allowed low-energy effective Hamiltonian that well captures the GC and count the number of fine-tuning parameters. Since \mathcal{G}_0 and the symmetry properties of the bands involved in the GC are fixed in one GC case, the form of the effective Hamiltonian can be unambiguously determined. (See details in Appendix B and C.) After obtaining the effective Hamiltonian, we can count the number of fine-tuning parameters required for each GC and select out all GC cases that require only 1 fine-tuning parameter (or equivalently has codimension 1), as shown in Fig. 1. Only these cases can be direct TQPTs between two gapped phases, since any two gapped states in the parameter space are adiabatically connected if 2 or more fine-tuning parameters are required to close the gap, and 0 codimension means there is a stable gapless phase in between two gapped phases. Our analysis shows that all GC cases in scenarios (i) for $p1$, (i) and (ii) for $p1m1$, $c1m1$, and $p1g1$, and (ii) for $p3m1$ and $p31m$ need 0 fine-tuning parameter or more than 1 fine-tuning parameters and thus cannot correspond to the direct TQPTs, while codimension-1 GC cases can exist in all other scenarios.

In the third and final step, we demonstrate the topological nature of all the codimension-1 GC cases by evaluating the change of certain topological invariants and derive the corresponding PET jump. As shown in Tab. 1, the Z_2 index is changed in all codimension-1 GC cases of scenarios (ii) for $p1$, (iii) for $p1m1$, $c1m1$, and $p1g1$, (i)-(iii) for $p3$, and (i) and (iii) for $p3m1$ and $p31m$, while the valley CN is changed for all codimension-1 GC cases of the scenarios (iv) for $p1m1$, $c1m1$, $p1g1$, $p3m1$, and $p31m$. We would like to emphasize that although valley CN itself is in general not quantized in a gapped phase, the change of valley CN across a gap closing is quantized and has physical consequence (46). (See the Methods for more details.) According to Fig. 1, the Z_2 cases either close the gap at TRIM or have an odd number of Dirac cones in half 1BZ, while all the valley CN cases (Fig. 1(d-e) and Fig. 1(n-o)) have an even number of Dirac cones in half 1BZ, forbidding the change of the Z_2 index. Nevertheless, no matter which type, they all lead to discontinuous changes of the symmetry-allowed PET components. (See detailed calculation of PET in Appendix B.)

In sum, we conclude that for all 7 PGs with non-vanishing PET, all the GC cases between two gapped phases with 1 fine-tuning parameter are direct TQPTs that change either Z_2 index or valley CN, and they all induce the discontinuous change of the symmetry-allowed PET components. Based on these results, we propose the following criteria to find realistic systems to test our theoretical predictions: (i) whether it breaks the 2D inversion or two-fold rotation with axis perpendicular to the 2D plane, (ii) whether it has significant SOC, and (iii) whether there is a tunable way to realize the GC. Applying these conditions to the existing material systems for 2D TQPT, we find two realistic material systems, namely the HgTe/CdTe QW and the layered material BaMnSb₂, which are studied in the following.

PGs	$p1$		$p1m1, c1m1, p1g1$				$p3$			$p3m1, p31m$			
Scenario	(i)	(ii)	(i)	(ii)	(iii)	(iv)	(i)	(ii)	(iii)	(i)	(ii)	(iii)	(iv)
Codim-1 GC	×	(a)	×	×	(b-c)	(d-e)	(f)	(g)	(h)	(i-j)	×	(k-m)	(n-o)
Topo. Inv.	N/A	Z_2	N/A	N/A	Z_2	VCN	Z_2	Z_2	Z_2	Z_2	N/A	Z_2	VCN
PET Jump	N/A	✓	N/A	N/A	✓	✓	✓	✓	✓	✓	N/A	✓	✓

Table 1: Summary for all 7 PGs with non-vanishing PET. The scenarios are classified by the symmetries that leave the GC momenta invariant, as shown in the Methods. Codim-1 GC means the GC cases with 1 fine-tuning parameter or codimension 1. If at least one GC case between gapped states with 1 fine-tuning parameter exists in the corresponding scenario, the subfigures in Fig. 1 that illustrate the GC momenta are referred to; otherwise, we fill in a \times . Topo. Inv. labels the topological invariant changed by the GC, Z_2 means the Z_2 index, and VCN means the corresponding case changes the valley CN when the valley is well-defined.

C. HgTe/CdTe Quantum Well

It has been demonstrated (6, 47) that the TQPT between the QSH insulator and NI phases in the HgTe/CdTe QW can be achieved by tuning the HgTe thickness d . Tuning applied electric field \mathcal{E} was theoretically predicted as an alternative way to achieve TQPT (48, 49), making the system an ideal platform to study the PET jump at TQPTs. Here, the stacking direction of the QW is chosen to be (111) instead of the well-studied (001) direction (50), since the latter would allow a two-fold rotation that forbids PET. Without the applied electric field, the (111) QW has the TR symmetry and the C_{3v} symmetries (generated by three-fold rotation along (111) and the mirror perpendicular to $(\bar{1}10)$); adding electric field along (111) does not change the symmetry properties. We should then expect one independent symmetry-allowed PET component γ_{222} similar to Eq. (B14) in the Methods, where 2 labels the direction $(11\bar{2})$.

The electronic band structure of the (111) QW can be described by the 6-band Kane model with the bases $(|\Gamma_6, \pm\frac{1}{2}\rangle, |\Gamma_8, \pm\frac{3}{2}\rangle, |\Gamma_8, \pm\frac{1}{2}\rangle)$. The electric field \mathcal{E} along (111) can be introduced by adding a linear electric potential that is independent of orbitals and spins. In this electron Hamiltonian, there are two inversion-breaking (IB) effects, the inherent IB effect in the Kane model and the applied electric field, and we neglect the former for simplicity. Note that such approximation does not lead to vanishing PET even for $\mathcal{E} = 0$ because the IB electron-strain coupling will be kept.

We first discuss the inversion-invariant $\mathcal{E} = 0$ case and focus on the PET jump induced by varying the width d . In this case, there are two double degenerate bands closest to the Fermi energy, namely $|E_1, \pm\rangle$ and $|H_1, \pm\rangle$ bands with opposite parities. With the method proposed in Ref. (6), we find that the gap between two bands closes at the Γ point around $d = 65\text{\AA}$ as shown in Fig. 2(a). The GC must be a Z_2 TQPT owing to the opposite parities of the two bands, and it belongs to scenario (i) of $p3m1/p31m$ discussed in Tab. 1 and the Methods. We further include the electron-strain coupling, and numerically plot the independent PET component γ_{222} as the function of the width in Fig. 2(b), which shows a jump around $d = 65\text{\AA}$. (See Appendix E.)

Next we study the TQPT induced by the applied electric field. In order to realize the GC at a nonzero value of the electric field, we fix the width of the QW at $d = 62\text{\AA}$, away from 65\AA . After adding the linear electric potential along (111) in the 6-band Kane model, we numerically find that the GC at Γ point happens at $\mathcal{E} \approx 0.0136\text{V \AA}^{-1}$, as shown in Fig. 2(c). Such GC belongs to scenario (i) of $p3m1/p31m$ and is still a Z_2 TQPT since the extra IB term cannot influence the Z_2 topology change. The PET component γ_{222} is numerically shown in Fig. 2(d), showing the jump across the TQPT. The PET jump in Fig. 2(b) and (d) has the order $10 \sim 100\text{pC m}^{-1}$, and thus is possible to be probed by the current experimental technique (51).

D. Layered Material BaMnSb₂

BaMnSb₂ is a 3D layered material that consists of Ba-Sb layers and Mn-Sb layers, which are stacked alternatively along the (001) direction (or equivalently z direction). The electrons in p_x and p_y orbitals of Sb atoms in the Ba-Sb layers account for the transport of the material. Owing to the insulating Mn-Sb layers, the tunneling along the z direction among different Ba-Sb layers is much weaker than the in-plane hopping terms, and thus BaMnSb₂ can be treated as a quasi-2D material (52). Therefore, we can only consider one Ba-Sb layer, whose structure is shown in Fig. 3(a). Owing to the zig-zag distortion of the Sb atoms (solid lines in Fig. 3(a)), the symmetry group that captures the main physics is spanned by the TR symmetry \mathcal{T} and two mirror operations m_y and m_z that are perpendicular

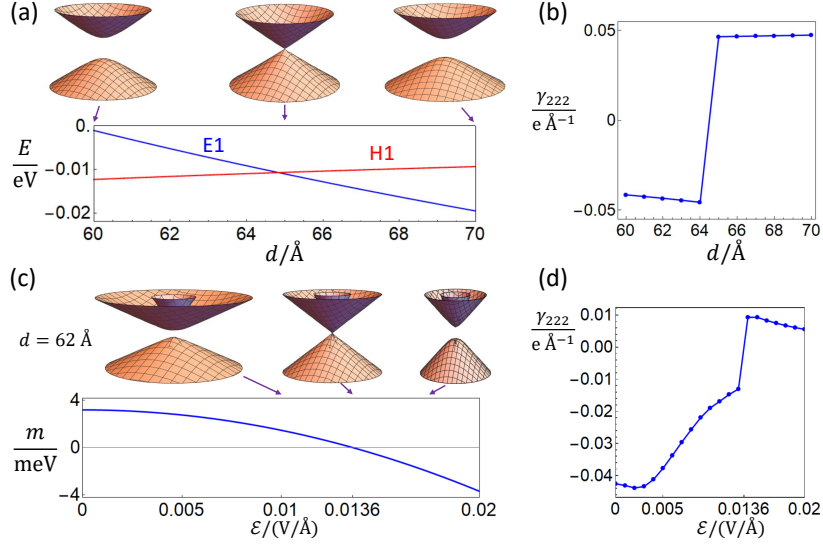


Fig 2: HgTe/CdTe QW. This figure shows the energy dispersion and the PET of the HgTe QW with the stacking direction (111). In (a), the lower panel shows the energy of E1 (blue) and H1 (red) bands at Γ point as a function of the width d , and the upper panel shows the energy dispersion at $d = 60, 65, 70$ Å from left to right, respectively. The GC happens around $d \approx 65$ Å, which is slightly different from the well-known $d = 63$ Å reported in Ref. (47) for the (001) stacking direction owing to the anisotropy effect. (b) shows the PET component γ_{222} as a function of d . In (c), the lower panel plots gap m as a function of the electric field \mathcal{E} with $d = 62$ Å, showing that the gap closes at $\mathcal{E} \approx 0.0136 \text{ VÅ}^{-1}$. The upper panel of (c) demonstrates the energy dispersion at $\mathcal{E} = 0.01, 0.0136, 0.017 \text{ VÅ}^{-1}$ from left to right, respectively. (d) shows the PET component γ_{222} as a function of \mathcal{E} .

to y and z axes, respectively. The mirror symmetry m_z does nothing but guarantee the z -component of the spin to be a good quantum number, allowing us to view the system as a spin-conserved TR-invariant 2D system with PG $p1m1$. Slightly different from the demonstration in the Methods, the mirror here is perpendicular to y instead of x , and thereby PG $p1m1$ now requires $\gamma_{yyy} = \gamma_{yxx} = \gamma_{xyx} = \gamma_{xxy} = 0$ and leaves the other four components as symmetry-allowed.

To describe this system, a tight-binding model with p_x and p_y orbitals of Sb atoms was constructed in Ref. (52) based on the first-principle calculation, and the form of the model is reviewed in Appendix F for integrity. This model qualitatively captures all the main features of the electronic band structure of BaMnSb₂. The key parameter of the model is the distortion parameter α that describes the zig-zag distortion of the Sb atoms. When α is tuned to a critical value $\alpha_c \approx 0.86$, the gap of the system closes at two valleys $\mathbf{K}_{\pm} = (\pi, \pm k_{y0})$ near X along $X - M$ in the BZ, as shown in Fig. 3(b). This GC results in a TQPT between the QSH state and the NI state in one Ba-Sb layer, as confirmed by the direct calculation of Z_2 index (Fig. 3(c)) according to expression in Ref. (53). Since the two GC momenta are invariant under $\mathcal{T}m_y$, this GC case satisfies the definition of scenario (iii) for $p1m1$. We further numerically verify the PET jump induced by the GC with the tight-binding model. The jump of the symmetry-allowed PET components is found at the TQPT around $\alpha = \alpha_c$ in Fig. 3(d), while the components forbidden by the symmetry stay zero. According to Fig. 3(d), both the jump and background are of the same order of magnitude, 0.1 eÅ^{-1} for $\gamma_{yxy, yyx}$ and 0.01 eÅ^{-1} for $\gamma_{xxx, xyy}$, indicating that the jump is experimentally measurable. The Z_2 topology change and the PET jump can also be analytically verified based on the effective model discussed in Appendix F.

III. DISCUSSION

In conclusion, we demonstrate that for all PGs that allow nonvanishing PET, the piezoelectric response has a discontinuous change across any TQPT in 2D TR invariant systems with significant SOC. Potential material realizations include the HgTe/CdTe quantum well and the layered material BaMnSb₂.

The early study on MoS₂ has demonstrated that the values of the PET obtained from the effective model might be (though not always) quite close to those from the first principles calculations (25). Therefore, although our theory is based on the effective Hamiltonian, the predicted jump of the PET is quite likely to be significant and even the sign change of PET, such as Fig. 2(b) and (d) for the HgTe case, might exist in realistic materials. The evaluation of the

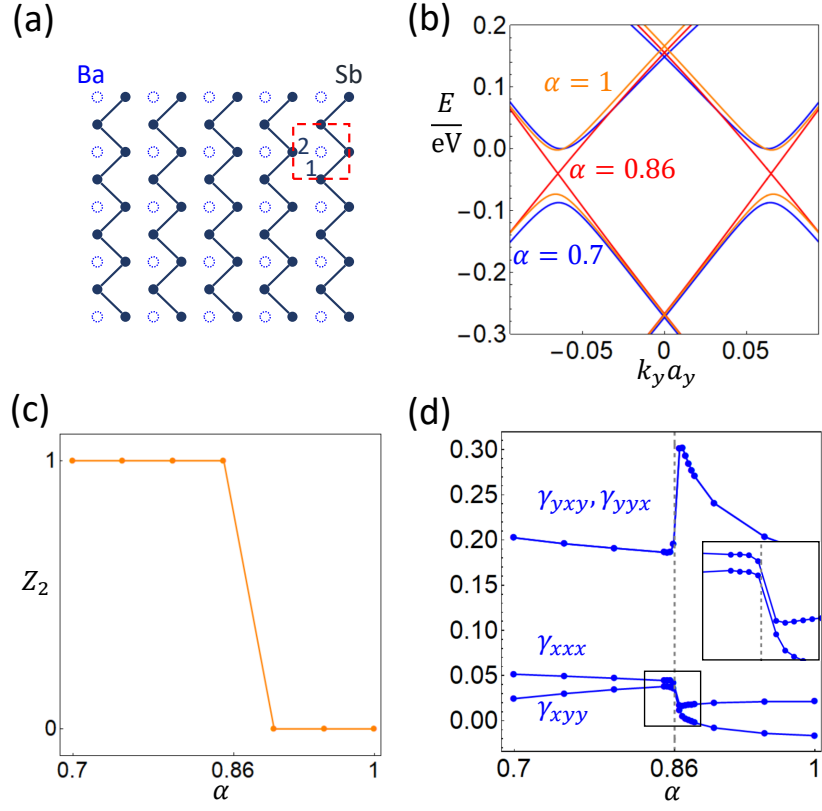


Fig 3: Layered Material BaMnSb₂. (a) illustrates the Ba-Sb layer, where each dashed circle stands for the projection of two Ba atoms onto the Sb layer and the solid dots are Sb atoms. The solid lines connecting Sb atoms indicate the zig-zag distortion, and the red dashed box marks the unit cell with 1 and 2 labeling the two Sb atoms. (b) The band structure of the TB model for BaMnSb₂ along $M - X - M$ for $\alpha = 0.86$ (red), $\alpha = 1$ (orange), and $\alpha = 0.7$ (blue), respectively, where X is at $k_y = 0$. (c) and (d) plot the Z_2 index and PET components obtained from the TB model as a function of α , respectively. In (d), the PET components are in the unit $\text{e}\text{\AA}^{-1}$, the gray dashed line is at $\alpha = 0.86$, and the inset is the zoom-in version of the boxed region.

PET from the first principles calculations is left for the future works.

Although we only focus on two realistic material systems in this work, the theory can be directly applied to other material systems. For example, the calculations for the HgTe/CdTe QW are also applicable to InAs/GaSb QWs, which share the same model (54). The QSH effect has also been observed in the monolayer 1T'-WTe₂ (55–57), but its inversion symmetry (58) forbids the piezoelectric effect. Therefore, a significant inversion breaking effect from the environment (such as substrate) is required to test our prediction in this system. While the SOC strength in graphene is small, it has been shown that the bilayer graphene sandwiched by TMDs has enhanced SOC and serves as a platform to observe TQPT (59, 60), where the PET jump is likely to exist. The piezoelectric effect has been observed in several 2D material systems (51, 61, 62), and therefore, the material systems and the experimental technique for the observation of the PET jump are both available. Since the PET jump is directly related to the TQPT, it further provides a new experimental approach to extract the critical exponents and universality behaviors of the TQPT, which can only be analyzed through transport measurements nowadays.

This work only focuses on 2D TR invariant systems with SOC, and the generalization to systems without SOC, without TR symmetry, or in 3D is left for the future. Despite the similarity between Eq. (3) and the expression of CN, the generalization to TR-breaking systems with non-zero CNs requires caution, due to the change of the definition of polarization (63). Another interesting question is whether the PET jump exists across the transition between states of different higher-order (64–67) or fragile topology (34, 68). We notice that although the dynamical piezoelectric effect may exist in metallic systems (69), its description is different from Eq. (3). It is thus intriguing to ask how the dynamical PET behaves across the transitions between insulating and semimetal phases.

IV. METHODS

A. Expression for the PET

According to Ref. (15 and 63), the expression for the PET of insulators, Eq. (3), is derived for systems with zero CNs and within the clamped-ion approximation where ions exactly follow the homogeneous deformation and thus cannot contribute to the PET. Even though the ion contribution might be non-zero in reality, the approximation is still legitimate in our study of PET jump since the ion contribution varies continuously across the GC of electronic bands.

Eq. (3) involves the derivative of the periodic part of the Bloch state $|\varphi_{n,\mathbf{k}}\rangle$ with respect to the strain tensor u_{jk} . $|\varphi_{n,\mathbf{k}}\rangle$ can always be expressed as $|\varphi_{n,\mathbf{k}}\rangle = \sum_{\mathbf{G}} f_{n,\mathbf{k},\mathbf{G}} |\mathbf{G}\rangle$ with \mathbf{G} the reciprocal lattice vector, and the derivative in fact means $|\partial_{u_{jk}} \varphi_{n,\mathbf{k}}\rangle \equiv \sum_{\mathbf{G}} (\partial_{u_{jk}} f_{n,\mathbf{k},\mathbf{G}}) |\mathbf{G}\rangle$ (15). In this way, the ill-defined $\partial_{u_{ij}} |\mathbf{G}\rangle$ is avoided, despite that $|\mathbf{G}\rangle$ is not continuous as changing the strain. If replacing the $|\partial_{u_{jk}} \varphi_{n,\mathbf{k}}\rangle$ in Eq. (3) by a momentum derivative $|\partial_{k_j} \varphi_{n,\mathbf{k}}\rangle$ with j different from i , the PET expression transforms into $-eC\epsilon^{ij}/(2\pi)$, where $\epsilon^{ij} = -\epsilon^{ji}$, $\epsilon^{xy} = 1$, and C is the Chern number of the 2D insulator (5)

$$C = \int \frac{d^2k}{2\pi} \sum_n F_{k_x, k_y}^n. \quad (13)$$

This reveals the similarity between the PET expression and the expression of the CN.

B. PG $p1$

For $p1$, no special constraints are imposed on the PET. There are two GC scenarios for the PG $p1$ with TR symmetry:

- (i) gap closes at TRIM ($\mathcal{T} \in \mathcal{G}_0$),
- (ii) gap closes not at TRIM ($\mathcal{T} \notin \mathcal{G}_0$).

In scenario (ii), \mathcal{G}_0 contains no symmetries other than the lattice translation, which we refer to as the trivial \mathcal{G}_0 .

C. PGs $p1m1$, $c1m1$, and $p1g1$

All three PGs, $p1m1$, $c1m1$, and $p1g1$, are generated by a mirror-related symmetry \mathcal{U} and the lattice translation. \mathcal{U} is a mirror operation for $p1m1/c1m1$ and a glide operation for $p1g1$. The difference between $p1m1$ and $c1m1$ lies on the directions of the primitive lattice vectors relative to the mirror line, which is not important for our discussion here. Without loss of generality, we choose the mirror or glide line to be perpendicular to x , labelled as m_x or g_x , respectively. The glide operation is thus denoted as $g_x = \{m_x | 0\frac{1}{2}\}$, where $0\frac{1}{2}$ represents the translation by half the primitive lattice vector along y . The \mathcal{U} symmetry in these three PGs requires

$$\gamma_{ijk} = (-1)^i (-1)^j (-1)^k \gamma_{ijk} \quad (14)$$

with $(-1)^x = -1$ and $(-1)^y = 1$, resulting that $\gamma_{xxx} = \gamma_{xyy} = \gamma_{yxy} = \gamma_{yyx} = 0$ while $\gamma_{xxy}, \gamma_{xyx}, \gamma_{yxx}, \gamma_{yyy}$ are allowed to be nonzero. For the symmetry analysis here, the PET behaves the same under the glide and mirror operations since u_{ij} is considered in the continuum limit. Based on \mathcal{G}_0 , we obtain in total 4 GC scenarios for these three PGs:

- (i) the GC at TRIM (\mathcal{G}_0 contains \mathcal{T}),
- (ii) \mathcal{G}_0 contains \mathcal{U} but not \mathcal{T} ,
- (iii) \mathcal{G}_0 contains \mathcal{UT} but not \mathcal{T} ,
- (iv) \mathcal{G}_0 is trivial.

D. PG $p3$

PG $p3$ is generated by 3-fold rotation C_3 and the lattice translation. Owing to C_3 , the PET satisfies the following relation

$$\gamma_{ijk} = \sum_{i'j'k'} [R(C_3)]_{ii'} [R(C_3)]_{jj'} [R(C_3)]_{kk'} \gamma_{i'j'k'} , \quad (15)$$

where

$$R(C_3) = \begin{pmatrix} -\frac{1}{2} & -\frac{\sqrt{3}}{2} \\ \frac{\sqrt{3}}{2} & -\frac{1}{2} \end{pmatrix} . \quad (16)$$

Solving the above equation gives two independent components γ_{xxx} and γ_{yyy} as

$$\begin{aligned} \gamma_{yxy} &= \gamma_{yyx} = \gamma_{xyy} = -\gamma_{xxx} \\ \gamma_{xxy} &= \gamma_{xyx} = \gamma_{yxx} = -\gamma_{yyy} . \end{aligned} \quad (17)$$

Again, we classify the GC for $p3$ according to \mathcal{G}_0 , resulting in three different scenarios:

- (i) \mathcal{G}_0 contains \mathcal{T} ,
- (ii) \mathcal{G}_0 contains C_3 but not \mathcal{T} ,
- (iii) \mathcal{G}_0 is trivial.

Here we do not have a scenario for \mathcal{G}_0 containing $C_3\mathcal{T}$ but no \mathcal{T} , since $(C_3\mathcal{T})^3$ is equivalent to \mathcal{T} .

E. PGs $p31m$ and $p3m1$

Both PGs $p31m$ and $p3m1$ are generated by the lattice translation, the three-fold rotation C_3 , and a mirror symmetry which we choose to be m_x without loss of generality. The difference between the two PGs lies on the direction of the mirror line relative to the primitive lattice vector: the mirror line is parallel or perpendicular to one primitive lattice vector for $p31m$ or $p3m1$, respectively. C_3 and m_x span the point group C_{3v} , which makes the PET satisfy Eq. (14) and Eq. (15). As a result, we have

$$\begin{aligned} \gamma_{xxx} &= \gamma_{xyy} = \gamma_{yxy} = \gamma_{yyx} = 0 \\ \gamma_{xyx} &= \gamma_{xxy} = \gamma_{yxx} = -\gamma_{yyy} \end{aligned} \quad (18)$$

for the PET, and thus γ_{yyy} serves as the only independent symmetry-allowed PET component. We classify the GC scenarios into 4 types according to \mathcal{G}_0 :

- (i) \mathcal{G}_0 contains \mathcal{T} ,
- (ii) \mathcal{G}_0 contains at least one of the three mirror symmetry operations in C_{3v} (again labeled as $\mathcal{U} = m_x, C_3m_x$, or $C_3^2m_x$) but no \mathcal{T} ,
- (iii) \mathcal{G}_0 contains \mathcal{UT} but no \mathcal{T} ,
- (iv) \mathcal{G}_0 is trivial.

F. Valley CN

In all the valley CN cases (Fig. 1(d,e,n,o)), the GC points locate at generic positions in the 1BZ. The valleys can be physically defined as the positions where the Berry curvature diverges as the gap approaches to zero. The positions of the Berry curvature peaks around the gap closing can be clearly seen in numerical calculations, as long as those peaks are well separated in the momentum space. (See Appendix D for more details.) With the positions of the valleys determined, the valley CN on one side of the GC is not necessarily quantized to integers since the integral of Berry curvature is not over a closed manifold. However, the change of valley CN across the GC is always integer-valued,

since it is equal to the CN of the Hamiltonian given by patching the two low-energy effective models on the two sides of the GC at large momenta, which lives on a closed manifold. One physical consequence of the quantized change of valley CN is the gapless domain-wall mode (46), which can be experimentally tested with transport or optical measurements (70). We verify the quantized change of valley CN and demonstrate the corresponding gapless domain-wall mode with a tight-binding model in Appendix D.

The above argument relies on the constraint that the valleys are well separated in 1BZ, preventing the two states from being adiabatically connected. Without the constraint of well-defined valleys, the valleys are allowed to be merged, and two phases with different valley CNs might be adiabatically connected. Therefore, we refer to the topology characterized by valley CN as locally stable (21), though globally unstable. Nevertheless, we restrict all valleys to be well-defined in our discussion and refer to the corresponding gap closing case as a TQPT.

V. ACKNOWLEDGEMENT

We are thankful for the helpful discussion with B. Andrei Bernevig, Xi Dai, F. Duncan M. Haldane, Shao-Kai Jian, Biao Lian, Xin Liu, Laurens W. Molenkamp, Zhiqiang Mao, Xiao-Qi Sun, David Vanderbilt, Jing Wang, Binghai Yan, Junyi Zhang, and Michael Zaletel. We acknowledge the support of the Office of Naval Research (Grant No. N00014-18-1-2793), the U.S. Department of Energy (Grant No. DESC0019064) and Kaufman New Initiative research grant KA2018-98553 of the Pittsburgh Foundation.

Appendix A: Derivation of the PET

In this section, we derive Eq. (3) in the main text via linear response theory from Eq. (2) in the main text, which is equivalent to the derivation in Ref. (15). The derivation is done with the natural unit $c = \hbar = 1$ and the metric $(-, +, +)$.

To apply the linear response theory, we start from an action S that includes the electronic effective model and the leading order effect of the infinitesimal strain. Since the current is present in Eq. (2), we should include the $U(1)$ gauge field that accounts for the electromagnetic field. With the $U(1)$ gauge field, the action reads

$$S = \int \frac{d^3k}{(2\pi)^3} \psi_k^\dagger G_0^{-1}(k) \psi_k + \int \frac{d^3k}{(2\pi)^3} \int \frac{d^3q}{(2\pi)^3} \left[\psi_{k+q/2}^\dagger \frac{\partial G_0^{-1}(k)}{\partial k^\mu} \psi_{k-q/2} eA^\mu(q) - \psi_{k+q/2}^\dagger M_{ij} \psi_{k-q/2} u_{ij}(q) \right], \quad (\text{A1})$$

where $k^\mu = (\omega, \mathbf{k})_\mu$, A^μ and u_{ij} and ψ follow the same Fourier transformation rule, $G_0(k) = [\omega - h_0(\mathbf{k})(1 - i\epsilon)]^{-1}$ is the time-ordered Green function without the electron-strain coupling, the chemical potential is chosen to be the zero energy, and M_{ij} is the matrix coupled to the strain tensor u_{ij} . To the leading order, the linear response is given by the following effective action

$$S_{eff} = \int d^3x \, e \partial_\nu A_\mu u_{ij} f^{ij,\mu\nu}, \quad (\text{A2})$$

where

$$f^{ij,\mu\nu} = -\frac{1}{2} \int \frac{d^3k}{(2\pi)^3} \{ \text{Tr} [G_0 \frac{\partial G_0^{-1}}{\partial k_\mu} G_0 \frac{\partial G_0^{-1}}{\partial k_\nu} G_0 M_{ij}] - (\mu \leftrightarrow \nu) \}, \quad (\text{A3})$$

and the absence of the Chern-Simons term AdA is due to the \mathcal{T} symmetry.

With Eq. (A2) and Eq. (2), we can use the condition that u_{ij} is uniform to derive the expression of the PET, resulting in

$$\gamma_{ijk} = -e f^{jk,i0}. \quad (\text{A4})$$

To further derive Eq. (3), we define $h(\mathbf{k}, u_{ij}) = h_0(\mathbf{k}) + u_{ij} M_{ij}$ and $G(k, u_{ij}) = [\omega - h(\mathbf{k}, u_{ij})(1 - i\epsilon)]^{-1}$ as the Hamiltonian and Green function with the electron-strain coupling, respectively. Using $\partial_{k_\mu} G^{-1} = \partial_{k_\mu} G_0^{-1}$ and $\partial_{u_{ij}} G^{-1} = -M_{ij}$, we can revise Eq. (A4) to

$$\gamma_{ijk} = \frac{e}{2} \int \frac{d^3k}{(2\pi)^3} \{ \text{Tr} [G \frac{\partial G^{-1}}{\partial k_i} G \frac{\partial G^{-1}}{\partial \omega} G \frac{\partial G^{-1}}{\partial u_{jk}}] - (k_i \leftrightarrow \omega) \} |_{u_{ij} \rightarrow 0}. \quad (\text{A5})$$

Define $X^\mu = (\omega, k_i, u_{jk})$ and then the above equation can be further transformed to

$$\gamma_{ijk} = -\frac{e}{3!} \int \frac{d^2 k d\omega}{(2\pi)^3} \epsilon^{\mu\nu\rho} \text{Tr} \left[G \frac{\partial G^{-1}}{\partial X^\mu} G \frac{\partial G^{-1}}{\partial X^\nu} G \frac{\partial G^{-1}}{\partial X^\rho} \right] \Big|_{u_{ij} \rightarrow 0}, \quad (\text{A6})$$

where $\epsilon^{\mu\nu\rho}$ is the Levi-Civita symbol. Integrating out ω in the above equation with the Wick rotation gives Eq. (3). Although the derivation here is done for $\hbar = c = 1$, all the expressions of γ_{ijk} and the resultant Eq. (3) stay the same after converting to the SI unit as they carry the right unit for the PET in 2+1D.

Finally, we would like to discuss the effect of the identity term of h_0 in Eq. (A2) when h_0 is a two band model. In general, the Hamiltonian can always be split into the identity part and the traceless part as $h_0(\mathbf{k}) = m_0(\mathbf{k})\mathbb{1} + h_0^{\text{traceless}}(\mathbf{k})$. The eigenvalues of $h_0(\mathbf{k})$ then read $m_0(\mathbf{k}) \pm \varepsilon(\mathbf{k})$, where $\pm\varepsilon(\mathbf{k})$ are two eigenvalues of $h_0^{\text{traceless}}(\mathbf{k})$ with $\varepsilon(\mathbf{k}) > 0$ chosen without loss of generality. As the model is gapped and the Fermi energy ($E = 0$) is chosen to lie inside the gap, we have $\varepsilon(\mathbf{k}) > |m_0(\mathbf{k})| \geq 0$. Since the poles of G_0 are at $\omega = [m_0(\mathbf{k}) \pm \varepsilon(\mathbf{k})](1 - i\epsilon)$, integrating ω along $(-\infty, \infty)$ in $f^{ij,\mu\nu}$ of Eq. (A2) gives the same result as integrating ω along $(-\infty + m_0(\mathbf{k})(1 - i\epsilon), \infty + m_0(\mathbf{k})(1 - i\epsilon))$ owing to the absence of poles in between the two paths. As a result, we can directly neglect the identity term of a two-band insulating h_0 in $f^{ij,\mu\nu}$ of Eq. (A2).

Appendix B: Details on PET for Each PG

The discussion on the electronic effective model and FTP of the gap closing between two non-degenerate states has some overlap with Ref. (45). However, the topological property and PET jump of the gap closing between two insulating states have not been discussed in Ref. (45).

1. PG $p1$

In the main text, the effective Hamiltonian for scenario (ii) of $p1$ is derived in a non-Cartesian coordinate system, which is not convenient for the generalization to other PGs with more crystalline symmetries. Thus, we re-derive the effective Hamiltonian in the Cartesian coordinate system, as given by (see Appendix. C1)

$$h_{\pm}(\mathbf{q}, u) = E_0(\pm\mathbf{q})\sigma_0 + (v_x q_x + v_0 q_y)\sigma_x + v_y q_y \sigma_y \pm m\sigma_z + \xi_{0,ij}\sigma_0 u_{ij} \pm \xi_{a',ij}\sigma_{a'} u_{ij}. \quad (\text{B1})$$

Here we only perform the unitary transformation on the bases of the Hamiltonian and do not rotate the momentum or the coordinate system. Correspondingly, the PET jump across the direct TQPT at $m = 0$ can be derived as

$$\begin{aligned} \Delta\gamma_{xij} &= -e \frac{\Delta N_+}{\pi} \frac{\xi_{y,ij}}{v_y} \\ \Delta\gamma_{yij} &= e \frac{\Delta N_+}{\pi} \left(\frac{\xi_{x,ij}}{v_x} - \frac{v_0}{v_x} \frac{\xi_{y,ij}}{v_y} \right). \end{aligned} \quad (\text{B2})$$

Eq. (B1)-(B2) resemble the conclusion for $p1$ in the Results and are useful for the discussion of the other 6 PGs with non-vanishing PET.

We would like to discuss more about the GC and PET for $p1$. In the first scenario, all TRIM have no essential differences and the gap closing always happens between two Kramers pairs unless more parameters are finely tuned. Therefore, there is no need to further classify this scenario into finer cases, and the codimension for the gap closing is 5, indicating that this scenario cannot be direct TQPT (26). According to the main text, no finer classification is needed for the second scenario either, the codimension of the gap closing scenario is 1, and it is indeed a direct TQPT that changes the Z_2 index and leads to the PET jump.

2. PGs $p1m1$, $c1m1$ and $p1g1$

In this part, we study three PGs, $p1m1$, $c1m1$, and $p1g1$, all of which are generated by a mirror-related symmetry \mathcal{U} and the lattice translation. \mathcal{U} is a mirror operation for $p1m1/c1m1$ and a glide operation for $p1g1$. The difference

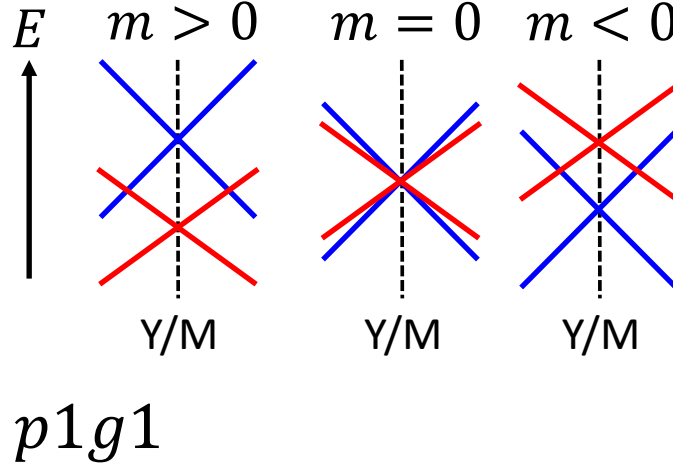


Fig 4: The figure shows the gap closing at Y or M in scenario (i) for $p1g1$. The lines indicate the band dispersion along k_y , and those in the same (different) colors have the same (opposite) g_x eigenvalues. m labels the gap at Y or M , and when the gap at Y or M is open ($m \neq 0$), the system is still in a gapless phase.

between $p1m1$ and $c1m1$ lies on the directions of the primitive lattice vectors relative to the mirror line, which is not important for our discussion here. Without loss of generality, we choose the mirror or glide line to be perpendicular to x , labelled as m_x or g_x , respectively. The glide operation is thus denoted as $g_x = \{m_x | 0\frac{1}{2}\}$, where “ $0\frac{1}{2}$ ” represents the translation by half the primitive lattice vector along y . The \mathcal{U} symmetry in these three PGs requires $\gamma_{xxx} = \gamma_{xyy} = \gamma_{yxy} = \gamma_{yyx} = 0$, whereas the PET components $\gamma_{xxy}, \gamma_{xyx}, \gamma_{yxx}, \gamma_{yyy}$ are allowed to be nonzero. For the symmetry analysis here, the PET behaves the same under the glide and mirror operations since u_{ij} is considered in the continuum limit.

In order to classify the gap closing scenarios, we define the group \mathcal{G}_0 for a gap closing momentum \mathbf{k}_0 such that \mathcal{G}_0 contains all symmetry operations that leave \mathbf{k}_0 invariant. Since \mathcal{G}_0 can include the TR-related operation, it can be larger than the little group of \mathbf{k}_0 . Based on \mathcal{G}_0 , we obtain in total 4 gap closing scenarios for these three PGs: (i) the gap closing at TRIM (\mathcal{G}_0 contains \mathcal{T}), (ii) \mathcal{G}_0 contains \mathcal{U} but not \mathcal{T} , (iii) \mathcal{G}_0 contains \mathcal{UT} but not \mathcal{T} , (iv) \mathcal{G}_0 contains no symmetries other than the lattice translation, which we refer to as the trivial \mathcal{G}_0 . As summarized in Tab. 1 in the main text, the TQPT exists in scenario (iii) and (iv), which can lead to the jump of symmetry-allowed PET components.

a. Scenario (i): TRIM

In scenario (i), the gap closing requires 3 (5) fine-tuning parameters (FTPs) for $p1m1$ and $c1m1$ if m_x is (is not) in the \mathcal{G}_0 . (See Appendix. C2.) For $p1g1$, the TRIM (Γ, X, Y and M) are split into two classes according to the value of g_x^2 : Γ, X with $g_x^2 = -1$ and Y, M with $g_x^2 = 1$. The gap closing at Γ, X needs 3 FTPs since g_x behaves the same as m_x , while the gap closing at Y, M needs only 1 FTP if it happens between two Kramers pairs with opposite g_x eigenvalues. However, such gap closing at Y, M is in between two g_x -protected gapless phases with codimension 0, where the bands with opposite g_x eigenvalues cross with each other at momenta other than Y, M as shown in Fig. 4. Therefore, there is no direct TQPT between two gapped phases in scenario (i).

b. Scenario (ii): $\mathcal{U} \in \mathcal{G}_0$ but $\mathcal{T} \notin \mathcal{G}_0$

The same situation occurs for scenario (ii). In scenario (ii), the gap closes at two different momenta $\pm\mathbf{k}_0$ that are invariant under the \mathcal{U} operation, meaning that the bases at $\pm\mathbf{k}_0$ can have definite \mathcal{U} eigenvalues. The gap closing between the two bases with the same \mathcal{U} eigenvalues requires 2 FTPs, as discussed in Appendix. C2. When the gap closes between two bands with opposite \mathcal{U} eigenvalues, the system always enters a stable \mathcal{U} -protected gapless phase with 0 codimension. (This case is not the same as the scenario (i) since only one side is guaranteed to be gapless.) Thus, the gap closing cases cannot be direct TQPTs.

c. Scenario (iii): $\mathcal{UT} \in \mathcal{G}_0$ but $\mathcal{T} \notin \mathcal{G}_0$

In scenario (iii), the gap closing occurs at two different momenta $\pm \mathbf{k}_0$ that are invariant under \mathcal{UT} , as shown by the orange dashed lines in Fig. 1 (b) and (c) in the main text.

For $p1m1$ and $c1m1$ ($\mathcal{U} = m_x$), $(m_x \mathcal{T})^2 = 1$ suggests that we can have $m_x \mathcal{T} \doteq \mathcal{K}$ at \mathbf{k}_0 by choosing the appropriate bases and the band touching point at \mathbf{k}_0 should typically occur between two non-degenerate bands. We further take $\mathcal{T} \doteq i\sigma_y \mathcal{K}$ by choosing the appropriate bases at $-\mathbf{k}_0$, and thus the two-band effective models $h_{\pm}(\mathbf{q}, u)$ at $\pm \mathbf{k}_0$ can be given by Eq. (B1) with extra constraints

$$v_0 = \xi_{a_1, xy} = \xi_{a_1, yx} = \xi_{y, xx} = \xi_{y, yy} = 0 \quad (\text{B3})$$

for $a_1 = 0, x, z$. As a result, only 1 FTP m is needed for the gap closing ($m = 0$), and only one single Dirac cone exists in half 1BZ at the transition, leading to the change of the Z_2 index. Based on Eq. (B2), the jump of symmetry-allowed PET components across this TQPT can be derived as

$$\begin{aligned} \Delta\gamma_{xxy} &= \Delta\gamma_{xyx} = -e \frac{\Delta N_+}{\pi} \frac{\xi_{y, xy}}{v_y} \\ \Delta\gamma_{yxx} &= e \frac{\Delta N_+}{\pi} \frac{\xi_{x, xx}}{v_x} \\ \Delta\gamma_{yyy} &= e \frac{\Delta N_+}{\pi} \frac{\xi_{x, yy}}{v_x}. \end{aligned} \quad (\text{B4})$$

For $p1g1$ with $\mathcal{U} = g_x$, since $(g_x \mathcal{T})^2 = 1$ at $(k_x, 0)$ and $(g_x \mathcal{T})^2 = -1$ at $(k_x, \pm\pi)$, we have two different gap closing cases. When the gap closes at $(\pm k_{0,x}, 0)$, the algebra relation involving $g_x \mathcal{T}$ is the same as $m_x \mathcal{T}$, *e.g.* $(g_x \mathcal{T})^2 = (m_x \mathcal{T})^2 = 1$, and thus the effective Hamiltonian can be chosen to be the same as that for $p1m1$ and $c1m1$, leading to 1 FTP, Z_2 index change, and the same form of PET jump. On the contrast, due to $(g_x \mathcal{T})^2 = -1$ at $(\pm k_{0,x}, \pm\pi)$, the gap closing needs 4 FTPs and thus no TQPT can occur in this case. (See Appendix. C2.)

d. Scenario (iv): trivial \mathcal{G}_0

In scenario (iv), the gap should close simultaneously at four momenta $\mathbf{k}_0, \mathbf{k}_1 = -\mathbf{k}_0, \mathbf{k}_2 = \mathcal{U}\mathbf{k}_0$, and $\mathbf{k}_3 = -\mathcal{U}\mathbf{k}_0$, as depicted in Fig. 1 (d) and (e) in the main text. The gap closing at \mathbf{k}_0 can be described by the Hamiltonian $h_+(\mathbf{q}, u)$ in Eq. (B1), and the Hamiltonian at $\mathbf{k}_1, \mathbf{k}_2$, and \mathbf{k}_3 can be given by $\mathcal{T}h_+(-\mathbf{q}, u)\mathcal{T}^\dagger, \mathcal{U}h_+(\mathcal{U}^{-1}\mathbf{q}, \mathcal{U}^{-1}u(\mathcal{U}^{-1})^T)\mathcal{U}^\dagger$, and $\mathcal{U}\mathcal{T}h_+(-\mathcal{U}^{-1}\mathbf{q}, \mathcal{U}^{-1}u(\mathcal{U}^{-1})^T)(\mathcal{UT})^\dagger$, respectively. Therefore, the gap closing can be achieved by tuning 1 FTP, *i.e.* m in $h_+(\mathbf{q}, u)$, in this scenario.

There is no change of Z_2 index for this scenario, since two Dirac cones exist in half 1BZ when the gap closes and the CN of contracted half 1BZ can only change by an even number. Nevertheless, scenario (iv) can still be “topological” in the context of valley Chern number (VCN) as elaborated in the following. Due to the Dirac Hamiltonian form shown in Eq. (B1), the Berry curvature is peaked at each valley $\mathbf{k}_{0,1,2,3}$ for a small m and can be captured by the electronic part of the corresponding effective Hamiltonian. Then, we can integrate the Berry curvature given by the effective model and get the VCN (20, 25) for each valley as $N_{\mathbf{k}_i} = -\eta_i \text{sgn}(v_x v_y) \text{sgn}(m)/2$ with $i = 0, 1, 2, 3$. The values of η_i at different valleys are related by the TR and \mathcal{U} symmetries, both of which flip the sign of the Berry curvature. Thus, we have $\eta_0 = \eta_3 = 1$ and $\eta_1 = \eta_2 = -1$. It should be pointed out that the Berry curvature integral is not over the entire 1BZ and the VCN at each valley thus does not need to be an integer. Nevertheless, the change of VCN across the gap closing is defined on a closed manifold and must be an integer number, given by $\Delta N_{\mathbf{k}_i} = -\eta_i \text{sgn}(v_x v_y)$ as varying m from 0^- to 0^+ . For the convenience of further discussion, we can define the VCN of the whole system (25) as $N_{\text{val}} = \sum_i \eta_i N_{\mathbf{k}_i} = -2 \text{sgn}(v_x v_y) \text{sgn}(m)$, and the change of the VCN becomes $\Delta N_{\text{val}} = -4 \text{sgn}(v_x v_y) = 4 \Delta N_+$ with the factor 4 for the four valleys. Therefore, if we restrict all the valleys to be far apart in the momentum space, the change of the VCN is a well-defined topological invariant and this gap closing scenario is a TQPT.

In principle, tuning parameters may merge different valleys at some high symmetry momentum, *e.g.* the valleys at \mathbf{k}_0 and $\mathcal{U}\mathbf{k}_0$ merged at the mirror or glide line. Therefore, without the constraint of well-defined valleys, two phases with different VCNs can share the same band topology and thus can be adiabatically connected. It means the topology characterized by VCN is “locally stable” (21), though globally unstable. Nevertheless, we restrict all valleys to be well-defined in our discussion and refer to the gap closing scenario as a TQPT.

Next we study the change of the PET components at this TQPT, which can be split into two parts: $\Delta\gamma^{(0)}$ originating from $\pm \mathbf{k}_0$ and $\Delta\gamma^{(1)}$ given by $\pm \mathcal{U}\mathbf{k}_0$. $\Delta\gamma^{(0)}$ equals to Eq. (B2) since the effective models at $\pm \mathbf{k}_0$ are the same as

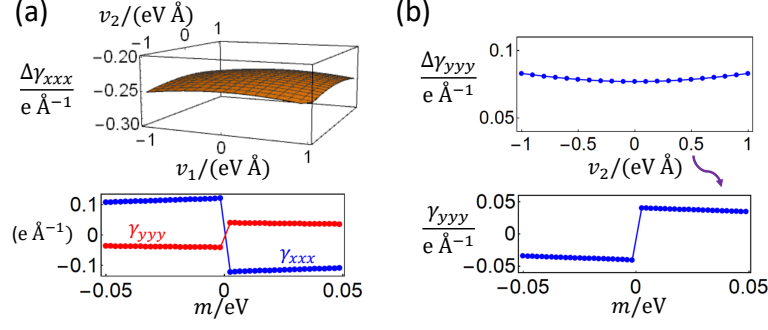


Fig 5: The upper panels of (a) and (b) numerically show the PET jump induced by the gap closing at Γ point as the function of $v_{1,2}$ and v_2 , respectively. The lower panels of (a) and (b) plot the PET component as a function of m for $(v_1, v_2) = (0.5, 0.5)\text{eV}\text{\AA}$ and $v_2 = 0.5\text{eV}\text{\AA}$, respectively.

Eq. (B1). Owing to the mirror or glide symmetry, $\Delta\gamma^{(1)}$ is related to $\Delta\gamma^{(0)}$ as $\Delta\gamma_{ijk}^{(1)} = (\mathcal{U})_{ii'}(\mathcal{U})_{jj'}(\mathcal{U})_{kk'}\gamma_{i'j'k'}^{(0)}$. As a result, we obtain the non-zero jump of symmetry-allowed PET components $\Delta\gamma_{ijk} = \Delta\gamma_{ijk}^{(0)} + \Delta\gamma_{ijk}^{(1)}$ as

$$\begin{aligned}\Delta\gamma_{xxy} &= \Delta\gamma_{xyx} = -e \frac{\Delta N_{\text{val}}}{2\pi v_y} \xi_{yxy} \\ \Delta\gamma_{yxx} &= -e \frac{\Delta N_{\text{val}}(-v_y \xi_{xxx} + v_0 \xi_{yxx})}{2\pi v_x v_y} \\ \Delta\gamma_{yyy} &= -e \frac{\Delta N_{\text{val}}(-v_y \xi_{xyy} + v_0 \xi_{yyy})}{2\pi v_x v_y}.\end{aligned}\tag{B5}$$

3. PG $p3$

PG $p3$ is generated by 3-fold rotation C_3 and the lattice translation. Owing to C_3 , the PET only has two independent components γ_{xxx} and γ_{yyy} as

$$\begin{aligned}\gamma_{xyy} &= \gamma_{yyx} = \gamma_{xyy} = -\gamma_{xxx} \\ \gamma_{xxy} &= \gamma_{xyx} = \gamma_{yxx} = -\gamma_{yyy}.\end{aligned}\tag{B6}$$

Again, we classify the gap closing for $p3$ according to \mathcal{G}_0 , resulting in three different scenarios: (i) \mathcal{G}_0 contains \mathcal{T} , (ii) \mathcal{G}_0 contains C_3 but not \mathcal{T} , and (iii) \mathcal{G}_0 is trivial. Here we do not have a scenario for \mathcal{G}_0 containing $C_3\mathcal{T}$ but no \mathcal{T} , since $(C_3\mathcal{T})^3$ is equivalent to \mathcal{T} . As summarized in Tab. 1 in the main text and elaborated in the following, in any of the above scenarios, there are gap closing cases between gapped states that need only 1 FTP, change the Z_2 index, and lead to the discontinuous change of symmetry-allowed PET components.

a. Scenario (i): TRIM

There are 4 TRIM in scenario (i), namely three M points related by C_3 and one Γ point, as labeled in Fig. 1 (f) in the main text. \mathcal{G}_0 of each individual M point only contains \mathcal{T} and the lattice translation, and thus the gap closing at M needs 5 FTPs, same as the gap closing at TRIM for $p1$.

When the gap closes at Γ point as shown in Fig. 1 (f) in the main text, \mathcal{G}_0 also contains C_3 with $C_3^3 = -1$. Due to $[C_3, \mathcal{T}] = 0$, the Kramers pairs can be classified into two types according to the C_3 eigenvalues: one with $(e^{-i\pi/3}, e^{i\pi/3})$ and the other with $(-1, -1)$. The gap closing between the Kramers pairs of the same type requires more than 1 FTPs, 3 for $(e^{-i\pi/3}, e^{i\pi/3})$ type and 5 for $(-1, -1)$ type, as discussed in Appendix. C3.

The gap closing with 1 FTP happens between the TR pairs of different types, for which the minimal four-band effective Hamiltonian in the bases $(e^{-i\pi/3}, e^{i\pi/3}, -1, -1)$ reads

$$h_{p3}(\mathbf{k}, u) = h_{p3,0}(\mathbf{k}) + h_{p3,1}(u),\tag{B7}$$

where $h_{p3,0}$ is the electron part

$$\begin{aligned}
h_{p3,0}(\mathbf{k}) = & E_0\tau_0\sigma_0 + m\tau_z\sigma_0 + (v_1k_x + v_2k_y)\left(\frac{\tau_0 + \tau_z}{2}\right)\sigma_x \\
& + (v_1k_y - v_2k_x)\left(\frac{\tau_0 + \tau_z}{2}\right)\sigma_y + (v_3k_x + v_4k_y)\tau_x\sigma_z \\
& + (-v_3k_y + v_4k_x)\tau_y\sigma_0 + (v_5k_x + v_6k_y)\tau_x\sigma_x \\
& + (-v_5k_y + v_6k_x)\tau_x\sigma_y,
\end{aligned} \tag{B8}$$

and $h_{p3,1}$ describes the electron-strain coupling

$$\begin{aligned}
h_{p3,1}(u) = & (u_{xx} + u_{yy})(\xi_1\tau_0\sigma_0 + \xi_2\tau_z\sigma_0) \\
& + (-u_{xx} + u_{yy})(\xi_3\tau_y\sigma_z + \xi_5\tau_y\sigma_x - \xi_4\tau_x\sigma_0 + \xi_6\tau_y\sigma_y) \\
& + (u_{xy} + u_{yx})(\xi_4\tau_y\sigma_z + \xi_6\tau_y\sigma_x + \xi_3\tau_x\sigma_0 - \xi_5\tau_y\sigma_y).
\end{aligned} \tag{B9}$$

τ 's and σ 's are Pauli matrices that label two different Kramers pairs and two components of each Kramers pair, respectively, m is the gap closing tuning parameter, and the bases are chosen such that $\mathcal{T} \doteq -i\tau_0\sigma_y\mathcal{K}$.

This gap closing is certainly a TQPT since it changes the numbers of IRs of the occupied bands, meaning that the two gapped states separated by this gap closing cannot be adiabatically connected. When $v_1 = v_2 = 0$, we can define an effective inversion symmetry $\tilde{P} = \tau_z\sigma_0$ for the electron part of Eq. (B7), $\tilde{P}h_{p3,0}(-\mathbf{k})\tilde{P}^\dagger = h_{p3,0}(\mathbf{k})$, and thus the gap closing of $h_{p3,0}(\mathbf{k})$ with $v_1 = v_2 = 0$ changes the Z_2 index according to the Fu-Kane criteria (71) since the parity of the occupied band changes. The existence of non-zero v_1, v_2 terms that break \tilde{P} cannot influence the Z_2 topology change, since (i) the Z_2 topology does not rely on the effective inversion symmetry, and (ii) additional gap closing away from Γ is forbidden at $m = 0$ as long as the $v_{1,2}$ terms are restored adiabatically. Therefore, within a certain range of $v_{1,2}$, the codimension-1 gap closing at $m = 0$ is a direct TQPT that changes the Z_2 index.

The remaining question is if the codimension-1 gap closing at $m = 0$ is always a Z_2 transition. To answer this question, note that we can always assume the transition at $m = 0$ is Z_2 for a parameter region S_1 of v_i 's in $h_{p3,0}$ and non- Z_2 for the other parameter region S_0 of v_i 's. Since the same form of the Hamiltonian can not correspond to Z_2 and non- Z_2 transitions simultaneously, the intersection of S_0 and S_1 is empty. Now we suppose both S_0 and S_1 are codimension-0 subspaces of the v_i parameter space (not the whole parameter space since only v_i 's are included while m is excluded). Then, the boundary of S_0 , labeled as ∂S_0 , is a codimension-1 subspace of v_i parameter space, and the special transition at $(m = 0, v_i \in \partial S_0)$ is a codimension-2 transition, as shown in Fig. 6.

Patching the Hamiltonian with $m = \pm\epsilon$ with ϵ positive and infinitesimal gives a Hamiltonian that lives on a closed manifold. This Hamiltonian has Z_2 trivial and nontrivial ground states when v_i 's are in S_0 and S_1 , respectively, as shown in Fig. 6. As v_i 's change from S_0 to S_1 passing through ∂S_0 , the patched Hamiltonian must experience a gap closing at generic \mathbf{k} points that changes Z_2 (Fig. 6), since there is always an energy gap at Γ for $m \neq 0$. As discussed with more detail in the following (see scenario (iii)), the gap closing at generic \mathbf{k} points surely changes the Z_2 index, is codimension-1, and simultaneously happens at six momenta. The gap closing can only happen either for $m = \epsilon$ part or for $m = -\epsilon$ part of the patched Hamiltonian but not both, since if the gap closes twice, the Z_2 index would be changed back. It means, the codimension-1 hypersurface for the gap closing at generic \mathbf{k} (red line in Fig. 6) touches the codimension-1 hypersurface for gap closing at Γ ($m = 0$ line in Fig. 6) just from one side of m but not passing through. As mentioned above, the touching part at $(m = 0, v_i \in \partial S_0)$ is a codimension-2 transition, owing to the assumption that both S_0 and S_1 are codimension-0 subspaces of v_i parameter space.

At the touching, we must have the six generic gap closing points merging at Γ . Otherwise, we should expect the red line in Fig. 6 to pass through the $m = 0$ line instead of stopping, since the gap closing process is local in the momentum space and different gap closing cases cannot influence each other if they happen at the different momenta. However, the merging process cannot be codimension-2 since moving a generic gap closing point to a specific momentum while keeping the gap closed requires at least 3 FTPs (two to move the momentum and one to close gap). Therefore, S_0 and S_1 cannot be both codimension-0 subspaces of v_i parameter space, and the codimension-1 gap closing at Γ can only be Z_2 or non- Z_2 but not both. Since we already show that the Z_2 transition at Γ can be codimension-1, the codimension-1 gap closing at Γ should always change the Z_2 index.

We next study the non-zero PET components, starting from the $v_1 = v_2 = 0$ case. If we further set $\xi_3 = \xi_4 = \xi_5 = \xi_6 = 0$, the electron-strain coupling $h_{p3,1}$ also has the effective inversion \tilde{P} , leading to the vanishing PET. It means

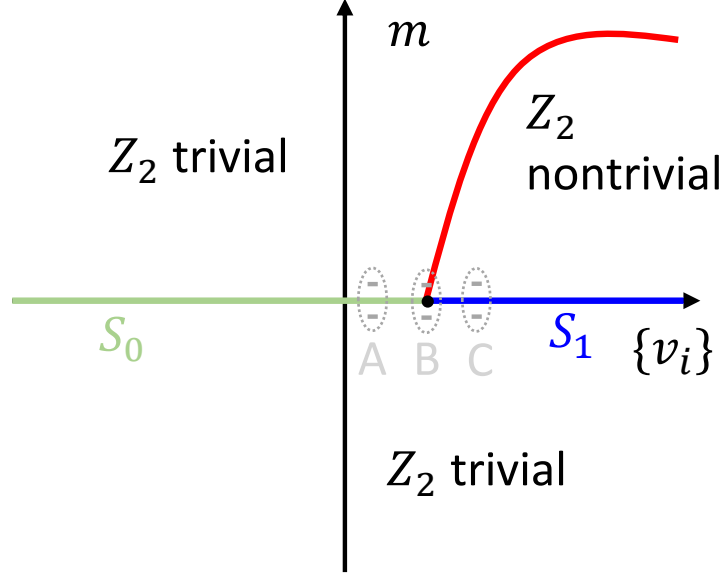


Fig 6: This figure shows the typical phase diagram around $(m = 0, v_i \in \partial S_0)$ (the black dot), within the assumption that both S_0 and S_1 are codimension-0 subspaces of the v_i parameter space. The green line is $(m = 0, v_i \in S_0)$ which does not change Z_2 index, the blue line is $(m = 0, v_i \in S_1)$ that changes Z_2 index, and the system closes the gap at six generic k points on the red line. Without loss of generality, we choose the red line to touch the $m = 0$ line from the positive m side. A, B, and C label three different Hamiltonians given by patching the two effective models with $m = \pm\epsilon$ at different values of v_i . A is Z_2 trivial, C is Z_2 non-trivial, and B closes the gap at the six generic k points for in $m = \epsilon$ part.

that ξ_1 and ξ_2 cannot contribute to the PET for $v_1 = v_2 = 0$. Indeed, the direct derivation gives the PET jump

$$\begin{aligned}\Delta\gamma_{xxx} &= -\frac{e}{\pi} \frac{\sum_{b=3}^6 v_b \xi_b}{\sum_{b=3}^6 v_b^2} \\ \Delta\gamma_{yyy} &= \frac{e}{\pi} \frac{v_4 \xi_3 - v_3 \xi_4 + v_6 \xi_5 - v_5 \xi_6}{\sum_{b=3}^6 v_b^2}.\end{aligned}\tag{B10}$$

For non-zero v_1 and v_2 , the PET components can be calculated numerically for $v_3 = v_4 = v_5 = v_6 = 1\text{eV\AA}$ and $\xi_1 = \xi_2 = \xi_3 = 2\xi_4 = \xi_5 = 2\xi_6 = 1\text{eV}$, showing the jump across the TQPT in Fig. 5(a).

b. Scenario (ii): $C_3 \in \mathcal{G}_0$ and $\mathcal{T} \notin \mathcal{G}_0$

The gap closing momenta in scenario (ii) are K and K' in Fig. 1 (g) in the main text. Since these two momenta are related by \mathcal{T} , we only need to derive the effective model at one momentum, say K , and the other one can be obtained using \mathcal{T} . At K , the C_3 symmetry has three possible eigenvalues $-1, e^{\pm i\pi/3}$ due to $C_3^3 = -1$. If the gap closing is between two states with the same C_3 eigenvalues, it cannot be TQPT since the fixed gap closing momentum leads to 3 FTPs for the gap closing. (See Appendix. C3.)

There are three cases for two states with different C_3 eigenvalues: $(e^{-i\pi/3}, e^{i\pi/3})$, $(e^{i\pi/3}, -1)$, and $(-1, e^{-i\pi/3})$. The effective models in the three cases are equivalent since the representations of C_3 in these cases can be related to each other by multiplying a phase factor $e^{\pm i2\pi/3}$. Therefore, we focus on the first case, of which the effective model at K (after an appropriate unitary transformation) is given by h_+ in Eq. (B1) with

$$\begin{aligned}v_x &= v_y \equiv v, \quad v_0 = 0, \quad \xi_{a'',xy} = \xi_{a'',yx} = 0, \\ \xi_{a'',xx} &= \xi_{a'',yy}, \quad \xi_{x,xx} = -\xi_{x,yy} = -\xi_{y,xy} = -\xi_{y,yx}, \\ \xi_{y,xx} &= -\xi_{y,yy} = \xi_{x,xy} = \xi_{x,yx},\end{aligned}\tag{B11}$$

where $a'' = 0$ or z . Similarly, by choosing the appropriate bases at K' such that $\mathcal{T} \doteq i\sigma_y \mathcal{K}$, the effective model at K' is given h_- in Eq. (B1) with the parameter relation listed above. As a result, the gap closing between states with

different C_3 eigenvalues needs 1 FTP and changes the Z_2 index since half 1BZ contains one Dirac cone (K or K'). Based on Eq. (B2), the jump of independent PET components across this TQPT (varying m from 0^- to 0^+) has the non-zero form

$$\Delta\gamma_{xxx} = -e \frac{\Delta N_+ \xi_{y,xx}}{\pi v}, \quad \Delta\gamma_{yyy} = e \frac{\Delta N_+ \xi_{x,yy}}{\pi v}, \quad (\text{B12})$$

where $\Delta N_+ = -\text{sgn}(v^2) = -1$.

c. Scenario (iii): trivial \mathcal{G}_0

In scenario (iii), there are six gap closing momenta, labeled as $\pm \mathbf{k}_0$, $\pm C_3 \mathbf{k}_0$ and $\pm C_3^2 \mathbf{k}_0$, as shown by red crosses in Fig. 1 (h) in the main text. The effective Hamiltonian at $\pm \mathbf{k}_0$ are exactly the same as Eq. (B1) since the two momenta are related by \mathcal{T} and no more symmetries are involved. Therefore, the gap closing scenario needs 1 FTP, and the contribution to the PET jump from the gap closing at $\pm \mathbf{k}_0$ is the same as Eq. (B2), noted as $\Delta\gamma_{ijk}^{(0)}$. The effective models at $\pm C_3 \mathbf{k}_0$ and $\pm C_3^2 \mathbf{k}_0$ can be obtained from those at $\pm \mathbf{k}_0$ by C_3 and C_3^2 operations, respectively, whose electronic parts are also in the Dirac Hamiltonian form. The contracted half 1BZ then contains three Dirac cones at the gap closing and its CN must change by an odd number, indicating the change of Z_2 index. Furthermore, the contributions to the jump of PET components from the gap closing at $\pm C_3 \mathbf{k}_0$ and $\pm C_3^2 \mathbf{k}_0$ are $\Delta\gamma_{ijk}^{(1)} = (C_3)_{ii'}(C_3)_{jj'}(C_3)_{kk'}\Delta\gamma_{i'j'k'}^{(0)}$, and $\Delta\gamma_{ijk}^{(2)} = (C_3^2)_{ii'}(C_3^2)_{jj'}(C_3^2)_{kk'}\Delta\gamma_{i'j'k'}^{(0)}$, respectively, owing to the symmetry. As a result, the jump of independent PET components is given by $\Delta\gamma_{ijk} = \Delta\gamma_{ijk}^{(0)} + \Delta\gamma_{ijk}^{(1)} + \Delta\gamma_{ijk}^{(2)}$, which has the nonzero form

$$\begin{aligned} \Delta\gamma_{xxx} &= -e \frac{3\Delta N_+}{4\pi} \frac{2v_y \xi_{x,xy} - 2v_0 \xi_{y,xy} + v_x(\xi_{y,xx} - \xi_{y,yy})}{v_x v_y} \\ \Delta\gamma_{yyy} &= e \frac{3\Delta N_+}{4\pi} \left[\frac{v_y(-\xi_{x,xx} + \xi_{x,yy}) + 2v_x \xi_{y,xy}}{v_x v_y} \right. \\ &\quad \left. + \frac{v_0(\xi_{y,xx} - \xi_{y,yy})}{v_x v_y} \right]. \end{aligned} \quad (\text{B13})$$

4. PG $p31m$ and PG $p3m1$

Both PGs $p31m$ and $p3m1$ are generated by the lattice translation, the three-fold rotation C_3 , and a mirror symmetry which we choose to be m_x without loss of generality. The difference between the two PGs lies on the direction of the mirror line relative to the primitive lattice vector: the mirror line is parallel or perpendicular to one primitive lattice vector for $p31m$ or $p3m1$, respectively. C_3 and m_x span the point group C_{3v} , which leads to

$$\begin{aligned} \gamma_{xxx} &= \gamma_{xyy} = \gamma_{yxy} = \gamma_{yyx} = 0 \\ \gamma_{xyx} &= \gamma_{xxy} = \gamma_{yxx} = -\gamma_{yyy} \end{aligned} \quad (\text{B14})$$

for the PET, and thus γ_{yyy} serves as the only independent symmetry-allowed PET component. We classify the gap closing scenarios into 4 types according to \mathcal{G}_0 : (i) \mathcal{G}_0 contains \mathcal{T} , (ii) \mathcal{G}_0 contains at least one of the three mirror symmetry operations in C_{3v} (again labeled as $\mathcal{U} = m_x$, $C_3 m_x$, or $C_3^2 m_x$) but no \mathcal{T} , (iii) \mathcal{G}_0 contains the \mathcal{UT} but no \mathcal{T} , and (iv) \mathcal{G}_0 is trivial. As summarized in Tab. 1 in the main text, all gap closing cases between gapped states with 1 FTP change either Z_2 index or the VCN, and lead to the jump of symmetry-allowed PET components.

a. Scenario (i): TRIM

Similar as Sec. B3a for PG $p3$, there are four inequivalent TRIM: the Γ point and three M points. Although \mathcal{G}_0 at the M point now contains \mathcal{U} , the gap closing still requires 3 FTPs same as the corresponding case in Sec. B2a, which cannot be a TQPT.

When the gap closes at Γ point (Fig. 1 (i-j) in the main text), the generators of \mathcal{G}_0 besides the lattice translation are C_3 , m_x and \mathcal{T} , and there are still two types of Kramers pairs characterized by the C_3 eigenvalues as those in Sec. B3a. Owing to the extra mirror symmetry here, the number of FTPs for the gap closing between the same type of Kramers pairs becomes 2 for $(e^{-i\pi/3}, e^{i\pi/3})$ type and 3 for $(-1, -1)$ type as discussed in Appendix. C4. Therefore,

we still only need to consider the gap closing between different types of Kramers pairs. For the convenience of the later material discussion, we choose the bases as $(e^{-i\pi/3}, -1, e^{i\pi/3}, -1)$. One can always choose the TR symmetry and mirror symmetry to be represented as $\mathcal{T} \doteq -i\sigma_y\tau_0\mathcal{K}$ and $m_x \doteq -i\sigma_x\tau_0$. In this case, the effective Hamiltonian can be derived by imposing the m_x on Eq. (B7), leading to

$$v_1 = v_4 = v_5 = \xi_3 = \xi_6 = 0. \quad (\text{B15})$$

The form of the Hamiltonian then reads

$$\begin{aligned} h_{p3m}(\mathbf{k}, u_{ij}) = & E_0 + \xi_1 u^2 \\ & + \begin{pmatrix} m & v_3 k_+ & i v_2 k_- & -i v_6 k_+ \\ v_3 k_- & -m & -i v_6 k_+ & 0 \\ -i v_2 k_+ & i v_6 k_- & m & -v_3 k_- \\ i v_6 k_- & 0 & -v_3 k_+ & -m \end{pmatrix} \\ & + \begin{pmatrix} \xi_2 u^2 & \xi_4 u_- & 0 & i \xi_5 u_- \\ \xi_4 u_+ & -\xi_2 u^2 & -i \xi_5 u_- & 0 \\ 0 & i \xi_5 u_+ & \xi_2 u^2 & \xi_4 u_+ \\ -i \xi_5 u_+ & 0 & \xi_4 u_- & -\xi_2 u^2 \end{pmatrix}, \end{aligned} \quad (\text{B16})$$

where $u^2 = u_{xx} + u_{yy}$, $u_{\pm} = u_{xx} - u_{yy} \pm i(u_{xy} + u_{yx})$.

The above Hamiltonian shows that the gap closing at Γ needs only 1 FTP, which is m . As discussed in Appendix. C 4, this gap closing cannot drive a gapped phase into a mirror-protected gapless phase, and therefore can separate two gapped states. Similar to the discussion in Sec. B 3 a, the gap closing changes the Z_2 index when tuning m from 0^- to 0^+ , indicating a TQPT. When $v_2 = 0$, an analytical expression for the jump of independent PET component can be obtained from Eq. (B10) and Eq. (B15), which reads

$$\Delta\gamma_{yyy} = \frac{e}{\pi} \frac{-v_3 \xi_4 + v_6 \xi_5}{v_3^2 + v_6^2}. \quad (\text{B17})$$

With parameter values $v_3 = v_6 = 1\text{eV}\text{\AA}$ and $\xi_1 = \xi_2 = 2\xi_4 = \xi_5 = 1\text{eV}$, the numerical results (Fig. 5(b)) for non-zero v_2 still show a PET jump across TQPT.

b. Scenario (ii): $\mathcal{U} \in \mathcal{G}_0$ and $\mathcal{T} \notin \mathcal{G}_0$

Scenario (ii) can be further divided into two classes depending on whether \mathcal{G}_0 contains C_3 . When \mathcal{G}_0 does not contain C_3 , the gap closing either requires more than 1 FTP or drives the system into a mirror-protected gapless phase with 0 codimension, similar to Sec. B 2 b.

Only when the gap closes at K, K' for $p31m$, \mathcal{G}_0 contains C_3 . In this case, \mathcal{G}_0 contains the group C_{3v} , which has one 2D irreducible representation (IR) and two different 1D IRs when acting on the states. The gap closing between the states furnishing the same IR requires 3 FTPs, similar to the case for two states with the same C_3 eigenvalue in Sec. B 3 b. If the gap closes between the doubly degenerate states furnishing the 2D IR and a state furnishing a 1D IR, the system with a fixed carrier density cannot be insulating on both sides of the gap closing because the number of occupied bands is changed. If the gap closes between two states that furnish different 1D IRs, the mirror-protected gapless phase must exist on one side of the gap closing as the two states must have opposite mirror eigenvalues. Therefore, there is no direct TQPT between the insulating phases in scenario (ii).

c. Scenario (iii): $\mathcal{UT} \in \mathcal{G}_0$ and $\mathcal{T} \notin \mathcal{G}_0$

In scenario (iii), the gap closing cases are again divided into two different classes depending on whether \mathcal{G}_0 has C_3 . We first discuss the class without C_3 , which happens for the gap closing at \mathcal{UT} invariant momenta except K, K' for $p3m1$. As shown in Fig. 1 (k-m) in the main text, the total number of inequivalent gap closing momenta is six, including $\pm\mathbf{k}_0$, $\pm C_3\mathbf{k}_0$, and $\pm C_3^2\mathbf{k}_0$. Without loss of generality, we choose \mathbf{k}_0 such that $-m_x\mathbf{k}_0$ is equivalent to \mathbf{k}_0 .

Then, the effective models at $\pm\mathbf{k}_0$ are the same as the corresponding models in Sec. B2c, *i.e.* Eq. (B1) with the parameter relation Eq. (B3), indicating 1 FTP for the gap closing. Since the effective models at $\pm C_3\mathbf{k}_0$ and $\pm C_3^2\mathbf{k}_0$ are related to those at $\pm\mathbf{k}_0$ by C_3 and C_3^2 operations similar to Sec. B3c, the jump of PET components can be derived by substituting Eq. (B3) into Eq. (B13), resulting in

$$\Delta\gamma_{yyy} = e^{\frac{3\Delta N_+}{4\pi} \frac{v_y(-\xi_{x,xx} + \xi_{x,yy}) + 2v_x\xi_{y,xy}}{v_x v_y}}. \quad (\text{B18})$$

Moreover, since three Dirac cones exist in half 1BZ when the gap closes, the Z_2 index changes at the gap closing, making it a TQPT.

The class that \mathcal{G}_0 includes C_3 can only happen when the gap closes at K and K' for PG $p3m1$, as shown in Fig. 1 (m) in the main text. We can choose C_3 and $m_x\mathcal{T}$ as the generators of \mathcal{G}_0 besides the lattice translation. Similar to Sec. B3b, we first study K and derive the model at K' by choosing the right bases such that $\mathcal{T} = i\sigma_y\mathcal{K}$. The states at K can be labeled by C_3 eigenvalues, -1 and $e^{\pm i\pi/3}$ given by $C_3^3 = -1$. Since $(m_x\mathcal{T})^2 = 1$ and $C_3 m_x\mathcal{T} = m_x\mathcal{T} C_3^{-1}$, the gap closing typically happens between two non-degenerate states, labeled by the C_3 eigenvalues as (λ_1, λ_2) , and we can always choose $m_x\mathcal{T} = \mathcal{K}$. The $\lambda_1 = \lambda_2$ case cannot correspond to TQPT since 2 FTPs are needed for the gap closing as discussed in Appendix. C4, while the $\lambda_1 \neq \lambda_2$ case requires only one FTP for the gap closing similar to Sec. B3b. Since the matrix representations of C_3 and $m_x\mathcal{T}$ are equivalent for the three choices $(\lambda_1, \lambda_2) = (e^{-i\pi/3}, e^{i\pi/3})$, $(e^{i\pi/3}, -1)$, and $(-1, e^{-i\pi/3})$, they have the same effective models and we only consider the first choice. With all the above conventions and simplifications, the effective models at K and K' can be given by those for Sec. B3b with an extra constraint $\xi_{y,yy} = 0$ brought by $m_x\mathcal{T}$. As a result, the Z_2 index does change when the gap closes, and the jump of PET components can be derived from Eq. (B12) with the above extra constraint, which reads

$$\Delta\gamma_{yyy} = -e^{\frac{\Delta N_+ \xi_{x,xx}}{\pi v}}. \quad (\text{B19})$$

d. Scenario (iv): trivial \mathcal{G}_0

In scenario (iv), the gap closes simultaneously at twelve inequivalent momenta, namely $\pm\mathbf{k}_0$, $\pm m_x\mathbf{k}_0$, $\pm C_3\mathbf{k}_0$, $\pm C_3 m_x\mathbf{k}_0$, $\pm C_3^2\mathbf{k}_0$ and $\pm C_3^2 m_x\mathbf{k}_0$ in Fig. 1 (n-o) in the main text. The effective model around \mathbf{k}_0 can be chosen as h_+ in Eq. (B1), and the models around other gap closing momenta can be further obtained by the symmetry. Although this gap closing scenario only needs 1 FTP, it cannot induce any change of Z_2 index since there is an even number (six) of Dirac cones in contracted half 1BZ. However, the gap closing can change the VCN when the twelve valleys are well defined according to Appendix. B2d, *e.g.* $N_{\mathbf{k}_0}$ can change by ± 1 , and thus is a TQPT in the sense of the locally stable topology.

We split the change of PET components for this scenario into 3 parts: $\gamma^{(0)}$ from $\pm\mathbf{k}_0$ and $\pm m_x\mathbf{k}_0$, $\gamma^{(1)}$ from $\pm C_3\mathbf{k}_0$ and $\pm C_3 m_x\mathbf{k}_0$, and $\gamma^{(2)}$ from $\pm C_3^2\mathbf{k}_0$ and $\pm C_3^2 m_x\mathbf{k}_0$. Since the contribution to $\gamma^{(0)}$ contains two Kramers pairs that are related by m_x , same as Sec. B2d, $\gamma^{(0)}$ equals to Eq. (B5). C_3 symmetry then gives $\Delta\gamma_{ijk}^{(1)} = (C_3)_{ii'}(C_3)_{jj'}(C_3)_{kk'}\Delta\gamma_{i'j'k'}^{(0)}$ and $\Delta\gamma_{ijk}^{(2)} = (C_3^2)_{ii'}(C_3^2)_{jj'}(C_3^2)_{kk'}\Delta\gamma_{i'j'k'}^{(0)}$, similar to Sec. B3c. As the result, the total change of PET can be obtained from $\Delta\gamma = \Delta\gamma^{(0)} + \Delta\gamma^{(1)} + \Delta\gamma^{(2)}$, which is proportional to the change of the VCN of the system

$$\Delta\gamma_{yyy} = e^{\frac{\Delta N_{\text{val}}}{8\pi} \left[\frac{v_y(-\xi_{x,xx} + \xi_{x,yy}) + 2v_x\xi_{y,xy}}{v_x v_y} + \frac{v_0(\xi_{y,xx} - \xi_{y,yy})}{v_x v_y} \right]} \quad (\text{B20})$$

with $\Delta N_{\text{val}} = 12\Delta N_+$.

5. 10 PGs with 2D Inversion or C_2

The PET jump cannot exist in 10 PGs that contain C_2 or inversion, including $p2$, $p2mm$, $p2mg$, $p2gg$, $c2mm$, $p4$, $p4mm$, $p4gm$, $p6$, and $p6mm$. This conclusion can be drawn from the symmetry analysis of PET. Since both C_2 and inversion transform (x, y) to $(-x, -y)$, $\gamma_{ijk} = -\gamma_{ijk}$ is required for those 10 PGs, leading to the vanishing PET. Early study (21, 44) also shows that a stable gapless phase can exist in between the QSH insulator and the NI when C_2 exists. In this gapless regime, 2D gapless Dirac fermions are locally stable and can only be created or annihilated in pairs.

Appendix C: Numbers of FTPs and Effective Models for the Gap Closing

The discussion on the gap closing between two non-degenerate states has some overlap with Ref. (45).

1. PG $p1$

This part has been studied in Ref. (26).

a. Not TRIM

When the gap closes at \mathbf{k}_0 that is not a TRIM, the two-band model near the gap closing to the leading order of $\mathbf{q} = \mathbf{k} - \mathbf{k}_0$ in general takes the form

$$h(\mathbf{q}) = E_0(\mathbf{q})\sigma_0 + (q_x\mathbf{C}_x + q_y\mathbf{C}_y + \mathbf{M}) \cdot \boldsymbol{\sigma} , \quad (\text{C1})$$

where $\mathbf{C}_i = (C_{ix}, C_{iy}, C_{iz})$, $\mathbf{M} = (M_x, M_y, M_z)$, $\boldsymbol{\sigma} = (\sigma_x, \sigma_y, \sigma_z)$, and the two bases of the above model account for the doubly degenerate band touching when the gap closes. Eq. (C1) determines the codimension for the gap closing scenario since the gap at $-\mathbf{k}_0$ is related to that of Eq. (C1) by the TR symmetry. The gap of Eq. (C1) closes if and only if $\mathbf{C}_x q_x + \mathbf{C}_y q_y + \mathbf{M} = 0$. We choose $\mathbf{C}_x \times \mathbf{C}_y \neq 0$ since it can be satisfied without finely tuning anything (or equivalently in a parameter subspace with 0 codimension). In this case, the gap closes when \mathbf{M} lies in the plane spanned by two vectors \mathbf{C}_x and \mathbf{C}_y . Therefore, the codimension for the gap closing is 1 since only the angle between the vector \mathbf{M} and the $(\mathbf{C}_x, \mathbf{C}_y)$ plane needs to be tuned.

Next, we derive Eq. (5) of the main text and the electronic part of h_+ in Eq. (B1), while the model at $-\mathbf{k}_0$ can be derived by the TR symmetry and thus is not discussed here. Eq. (C1) always allows the \mathbf{q} -independent SU(2) transformation, *i.e.* $h(\mathbf{q}) \rightarrow U^\dagger h(\mathbf{q}) U$ with $U \in \text{SU}(2)$. Such transformation only changes the bases of the Hamiltonian but does not change the direction of the momentum or the coordinate system. Since $\boldsymbol{\sigma}$ behaves as an SO(3) vector under U , every SU(2) transformation U of the Hamiltonian is equivalent to an SO(3) transformation R of the vectors \mathbf{C}_i and \mathbf{M} , *i.e.* $\mathbf{C}_i \rightarrow R\mathbf{C}_i$ and $\mathbf{M} \rightarrow R\mathbf{M}$. Thus, by choosing appropriate U matrix, we can first rotate \mathbf{C}_x to the x direction and then \mathbf{C}_y to the xy plane, resulting in $R\mathbf{C}_x = v_x\mathbf{e}_x$, $R\mathbf{C}_y = v_0\mathbf{e}_x + v_y\mathbf{e}_y$ and $R\mathbf{M} = m_1\mathbf{e}_x + m_2\mathbf{e}_y + m\mathbf{e}_z$. As a result, Eq. (C1) is transformed to

$$h(\mathbf{q}) = E_0(\mathbf{q})\sigma_0 + (v_x q_x + v_0 q_y + m_1)\sigma_x + (v_y q_y + m_2)\sigma_y + m\sigma_z . \quad (\text{C2})$$

Here $\mathbf{C}_x \times \mathbf{C}_y \neq 0$ gives non-zero v_x and v_y . With a shift of \mathbf{k}_0 by $(m_1/v_x - v_0 m_2/(v_x v_y), m_2/v_y)$, the model is further simplified to the electronic part of h_+ in Eq. (B1). Finally, we define the $q_x + v_0 q_y$ and q_y to be q_1 and q_2 , respectively, to get Eq. (5), which represents the most generic form of the Hamiltonian.

b. TRIM

In this part, we count the number of FTPs for the gap closing at the TRIM. Owing to the Kramers' degeneracy, every band at the TRIM is doubly degenerate, and we use the name "Kramers pair" to label the two states related by the TR symmetry. We consider the gap closing between two Kramers pairs $|1, \pm\rangle$ and $|2, \pm\rangle$, where $\mathcal{T}|i, +\rangle = -|i, -\rangle$ can always be chosen by the unitary transformation. As a result, the mass term for the effective model at the TRIM reads

$$\begin{pmatrix} m_1 & 0 & \Delta_0 + i\Delta_3 & i\Delta_1 + \Delta_2 \\ 0 & m_1 & i\Delta_1 - \Delta_2 & \Delta_0 - i\Delta_3 \\ \Delta_0 - i\Delta_3 & -i\Delta_1 - \Delta_2 & m_2 & 0 \\ -i\Delta_1 + \Delta_2 & \Delta_0 + i\Delta_3 & 0 & m_2 \end{pmatrix} \quad (\text{C3})$$

where the bases are $(|1, +\rangle, |1, -\rangle, |2, +\rangle, |2, -\rangle)$ and all parameters are real. Since the momentum is fixed at TRIM ($-\mathbf{k} = \mathbf{k} + \mathbf{G}$ with \mathbf{G} a reciprocal lattice vector), none of the terms in the above equation can be canceled by shifting the momentum. Therefore, 5 FTPs are needed for the gap closing.

2. $p1m1$, $c1m1$, and $p1g1$

a. Scenario (i): TRIM

If \mathcal{G}_0 does not contain \mathcal{U} , which can occur on the edge of 1BZ for $c1m1$, the situation is the same as the TRIM in Appendix. C1, which requires 5 FTPs. When \mathcal{G}_0 contains \mathcal{U} , we should discuss the $\mathcal{U} = m_x$ case ($p1m1$ and $c1m1$) and the $\mathcal{U} = g_x$ case ($p1g1$), separately.

For $p1m1$ and $c1m1$, since $m_x^2 = -1$, two states of one Kramers pair have opposite mirror eigenvalues $\pm i$, labeled by $m_x|i, \pm\rangle = \pm i|i, \pm\rangle$. On the bases ($|1, +\rangle, |1, -\rangle, |2, +\rangle, |2, -\rangle$), the effective model around the gap closing between two Kramers pairs can be given by Eq. (C3) with $\Delta_1 = \Delta_2 = 0$, since the bases with different mirror eigenvalues cannot be coupled by the mass terms. As a result, 3 FTPs are needed for such gap closing scenario.

For $p1g1$, $g_x^2 = -1$ at Γ and X and the number of FTPs for the gap closing is thus the same as the above case, which is 3. At Y and M , $g_x^2 = 1$ and two states of one Kramers pair have the same g_x eigenvalue, 1 or -1 . In this case, the gap closing between two Kramers pairs with the same g_x eigenvalue needs 5 FTPs, which is the same as the TRIM scenario in Appendix. C1. On the other hand, between two Kramers pairs with opposite g_x eigenvalues, only 1 FTP needs to be tuned to close the gap at Y or M , since the off-diagonal terms ($\Delta_{0,1,2,3}$) in Eq. (C3) are all forbidden.

b. Scenario (ii): $\mathcal{U} \in \mathcal{G}_0$ but $\mathcal{T} \notin \mathcal{G}_0$

In scenario (ii), there are two gap closing momenta $\pm \mathbf{k}_0$ that are related by the TR symmetry. Therefore, we only need to consider one of them, say \mathbf{k}_0 , to derive the number of FPTs for the gap closing. At \mathbf{k}_0 , the states can be labeled by the eigenvalues of \mathcal{U} . If the gap closing between two states with the same \mathcal{U} eigenvalues, the effective model can be described by Eq. (C1) with $|\mathbf{C}_x| = 0$. The gap closes if and only if $\mathbf{C}_y q_y + \mathbf{M} = 0$, realizable by making two vectors \mathbf{M} and \mathbf{C}_y parallel. Such realization needs 2 FTPs, *e.g.* the two components of the projection of \mathbf{M} on the plane perpendicular to \mathbf{C}_y .

When the gap closes between two states with different \mathcal{U} eigenvalues, the effective model along the \mathcal{U} -invariant line ($q_x = 0$) reads $h(\mathbf{q}) = E_0(q_y) + (m_0 + Cq_y + B_0q_y^2)\sigma_z$, which, by shifting the $k_{0,y}$, can be simplified to $h(\mathbf{q}) = E_0(q_y) + (m + Bq_y^2)\sigma_z$. The gap for this Hamiltonian keeps closing when $mB \leq 0$, indicating a stable gapless phase protected by \mathcal{U} with 0 codimension.

c. Scenario (iii): $\mathcal{UT} \in \mathcal{G}_0$ but $\mathcal{T} \notin \mathcal{G}_0$

In this scenario, we here only consider the $(\mathcal{UT})^2 = -1$ case, where each band at the gap closing momentum is doubly degenerate. We can define the \mathcal{UT} pair as the two degenerate states related by \mathcal{UT} , in analog to the Kramers pair defined in Appendix. C1. Similar as Eq. (C3), there are 5 mass terms for the gap closing between two \mathcal{UT} pairs. However, the case here is different from the TRIM scenario in Appendix. C1, since q_x does not change under \mathcal{UT} and thus the corresponding terms have the same form as the mass terms in Eq. (C3). One of the five mass terms can then be canceled by shifting $k_{0,x}$, resulting in 4 FTPs for the gap closing.

3. p_3

a. Scenario (i): TRIM

We first discuss the gap closing at Γ between two Kramers pairs of the same type. If the bases have C_3 eigenvalues ($e^{-i\pi/3}, e^{i\pi/3}, e^{-i\pi/3}, e^{i\pi/3}$), the mass term of the effective model is given by Eq. (C3) with $\Delta_1 = \Delta_2 = 0$ since the bases with different C_3 eigenvalues cannot be coupled, resulting in 3 FTPs for the gap closing. If the bases have C_3 eigenvalues $(-1, -1, -1, -1)$, the effective model equals to Eq. (C3) that has 5 FTPs for the gap closing.

Now we discuss the construction of the effective model for the bases ($e^{-i\pi/3}, e^{i\pi/3}, -1, -1$). The form of the effective model, Eq. (B7), is given by the tensor product of the bases in the same IR listed in Tab. 2. Note that the matrix representation and the bases for the E IR are not Hermitian. It means given two copies of $(E, +)$ or $(E, -)$ IR, say $(\tau_+(\sigma_x - i\sigma_y), \tau_+(\sigma_x + i\sigma_y))$ and $(k_x - ik_y, k_x + ik_y)$ furnishing $(E, -)$ IR, the coefficients used for the tensor product can be complex, *e.g.* $c[\tau_+(\sigma_x - i\sigma_y)][k_x - ik_y]^* + c^*[\tau_+(\sigma_x + i\sigma_y)][k_x + ik_y]^*$ with complex c .

IR	Expressions
$A_1, +$	$\tau_+ \sigma_0, \tau_- \sigma_0, u_{11} + u_{22}$
$A_1, -$	$\tau_+ \sigma_z, \tau_- \sigma_x, \tau_- \sigma_y, \tau_- \sigma_z$
$E, +$	$(\tau_y \sigma_z - i\tau_x \sigma_0, \tau_y \sigma_z + i\tau_x \sigma_0), (\tau_y \sigma_x + i\tau_y \sigma_y, \tau_y \sigma_x - i\tau_y \sigma_y), (-u_{xx} + u_{yy} - i(u_{xy} + u_{yx}), -u_{xx} + u_{yy} + i(u_{xy} + u_{yx}))$
$E, -$	$(\tau_+(\sigma_x - i\sigma_y), \tau_+(\sigma_x + i\sigma_y)), (\tau_x \sigma_z + i\tau_y \sigma_0, \tau_x \sigma_z - i\tau_y \sigma_0), (\tau_x \sigma_x + i\tau_x \sigma_y, \tau_x \sigma_x - i\tau_x \sigma_y), (k_x - ik_y, k_x + ik_y)$

Table 2: The irreducible representations (IRs) of C_3 and TR symmetries. In A_1 IR, the C_3 eigenvalue of the bases is 1 and \pm are parity under TR. “ E, \pm ” label two 2D IRs, where the two components have the C_3 eigenvalues $(e^{i2\pi/3}, e^{-i2\pi/3})$ and transform as $\pm \sigma_x \mathcal{K}$ under the TR symmetry. $\tau_{\pm} = (\tau_0 \pm \tau_z)/2$.

b. Scenario (ii): $C_3 \in \mathcal{G}_0$ and $\mathcal{T} \notin \mathcal{G}_0$

Here we consider the gap closing between two states with the same C_3 eigenvalues at K or K' . In general, the mass terms at one gap closing momentum are $m_x \sigma_x + m_y \sigma_y + m_z \sigma_z$. Since the gap closing momentum is fixed, none of the three mass terms can be canceled by shifting the momentum, and hence there are 3 FTPs for the gap closing.

4. $p31m$ and $p3m1$

a. Scenario (i): TRIM

When the two Kramers pairs carry C_3 eigenvalues as $(e^{-i\pi/3}, e^{i\pi/3}, e^{-i\pi/3}, e^{i\pi/3})$, the effective model equals to Eq. (C3) with $\Delta_1 = \Delta_2 = 0$ before considering m_x , similar to the correspond case in Appendix. C3. As $m_x \doteq -i\sigma_x$ for each Kramers pair, the Δ_3 is also forbidden, resulting in 2 FTPs for the gap closing. On the other hand, if C_3 eigenvalues are all -1 , the effective model equals to Eq. (C3) before considering m_x , similar to the correspond case in Appendix. C3, and including m_x makes $\Delta_2 = \Delta_3 = 0$, leading to 3 FTPs for the gap closing.

The construction of the effective model for the bases $(e^{-i\pi/3}, -1, e^{i\pi/3}, -1)$ is the same as that for the (111) HgTe/CdTe quantum well, which is discussed in Appendix. E. Next we show that the gap closing at Γ in this case cannot drive a gapped system to the mirror protected gapless phase. Since the three mirror lines are related by the C_3 symmetry, we only need to consider one of them, say $k_x = 0$ that is invariant under m_x . The eigenvalues along this line read

$$E_{\alpha\beta} = E_0 + \alpha \frac{k_y v_2}{2} + \beta \sqrt{(m + \alpha \frac{v_2 k_y}{2})^2 + k_y^2 (v_3^2 + v_6^2)} \quad (C4)$$

with α, β take \pm . $E_{\pm\beta}$ bands cross at Γ and belong to the same set of connected bands. The mirror eigenvalue of the $E_{\alpha\beta}$ band is $-\alpha i$, and then the mirror protected gapless phase happens when E_{++} crosses with E_{--} or E_{+-} crosses with E_{-+} . Both band crossings require the same condition

$$|v_2 k_y| = \sum_{\alpha} \sqrt{(m + \alpha \frac{v_2 k_y}{2})^2 + k_y^2 (v_3^2 + v_6^2)}, \quad (C5)$$

since they are related by the TR symmetry. However, the above equation has no solution when $m \neq 0$ and $v_3^2 + v_6^2 \neq 0$. It can be seen from the inequality $\sqrt{(a+b)^2 + c^2} + \sqrt{(a-b)^2 + c^2} > 2|b|$, which holds unless $c = 0$ and $|a| \leq |b|$. Therefore, without finely tuning more parameters to realize $v_3^2 + v_6^2 = 0$, a gapped system remains when the sign of m flips.

b. Scenario (iii): $\mathcal{UT} \in \mathcal{G}_0$ and $\mathcal{T} \notin \mathcal{G}_0$

Here we discuss the case when the gap closes at K and K' for PG $p3m1$ and between two states with the same C_3 eigenvalues. Before considering $m_x \mathcal{T}$, the mass terms at K are $m_x \sigma_x + m_y \sigma_y + m_z \sigma_z$ since C_3 does not provide any constraints and the fixed gap closing momentum cannot be shifted to cancel any of them. Since $m_x \mathcal{T}$ can be chosen as $\sigma_0 \mathcal{K}$, m_y is forbidden and the remaining two mass terms serve as the 2 FTPs for the gap closing.

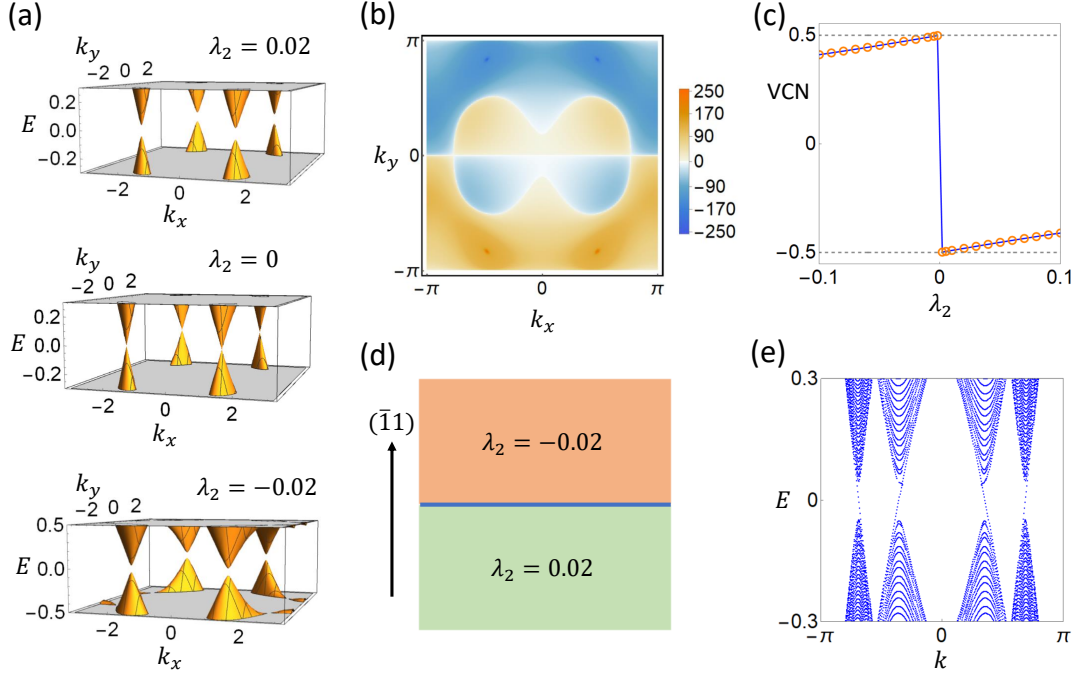


Fig 7: (a) shows the energy dispersion of the TB model Eq. (D3) for $\lambda_2 = 0.02, 0, -0.02$. The gap is zero for $\lambda_2 = 0$. (b) shows the distribution of the Berry curvature for $\lambda_2 = 0.02$. The peaks indicate the locations of valleys. (c) shows the integration of Berry curvature divided by 2π over the $k_{x,y} > 0$ quarter of 1BZ. The orange circles are the data points, based on which the blue line is plotted. (d) is a domain wall structure along $(\bar{1}1)$ direction. The lower and upper parts are given by the TB models for $\lambda_2 = -0.02$ and $\lambda_2 = 0.02$, respectively. (e) plots the energy dispersion of domain-wall modes (modes with considerable probability near the interface in (d)). Here we choose the number of unit cells along $(\bar{1}1)$ to be 70 for each part of the domain wall.

Appendix D: VCN in Tight-Binding Model

In this section, we discuss the quantization and physical meaning of the VCN change in a tight-binding (TB) model with $p1m1$. We consider a square lattice and each unit cell only contains one atom. Without loss of generality, we set the lattice constant to 1, and choose the mirror symmetry as m_y . On each atom, we include a spinful s and a spinful p_y orbitals, meaning that the bases can be labeled as $|\mathbf{R}, \alpha, s\rangle$ with \mathbf{R} the lattice vector, $\alpha = s, p_y$ for orbital, and $s = \uparrow, \downarrow$ for spin. The bases with specific Bloch momentum can be obtained by the following Fourier transformation

$$|\mathbf{k}, \alpha, s\rangle = \frac{1}{\sqrt{N}} \sum_{\mathbf{R}} e^{i\mathbf{k} \cdot \mathbf{R}} |\mathbf{R}, \alpha, s\rangle. \quad (\text{D1})$$

Then, the representations of the symmetries read

$$\begin{aligned} m_y |\mathbf{k}, \alpha, s\rangle &= |m_y \mathbf{k}, \alpha', s'\rangle (\tau_z)_{\alpha' \alpha} (-i\sigma_y)_{s' s} \\ \mathcal{T} |\mathbf{k}, \alpha, s\rangle &= |-\mathbf{k}, \alpha, s'\rangle (i\sigma_y)_{s' s}, \end{aligned} \quad (\text{D2})$$

where τ and σ are Pauli matrices for orbital and spin.

With on-site terms and nearest-neighbor hopping terms, we choose the following symmetry-allowed expression for the Hamiltonian

$$h(\mathbf{k}) = d_1 \tau_z \sigma_0 + d_2 \tau_y \sigma_z + d_3 \tau_x \sigma_z + d_4 \tau_y \sigma_0, \quad (\text{D3})$$

where

$$\begin{aligned} d_1 &= m + 2t_1 \cos(k_x) + 2t_2 \cos(k_y) \\ d_2 &= \lambda_1 \\ d_3 &= 2\lambda_2 \sin(k_x) \\ d_4 &= 2t_3 \sin(k_y). \end{aligned} \quad (\text{D4})$$

The eigenvalues of $h(\mathbf{k})$ read $\pm\sqrt{d_1^2 + d_3^2 + (d_2 \pm d_4)^2}$. For concreteness, we choose $t_1 = t_2 = t_3 = \lambda_1 = 1/2$ and $m = 4/5$ and assume the model is half-filled (two occupied bands). In this case, the gap closes only when we tune λ_2 to zero, as shown in Fig. 7(a), and the gap closing points sit at $\mathbf{k} = (\pm \arccos(\frac{-8+5\sqrt{3}}{10}), \pm 5\pi/6) \approx (\pm 1.50, \pm 2.62)$, belonging to the VCN scenario (iv) for $p1m1$. When the gap is small but nonzero, the positions of valleys can be determined numerically by locating the peaks of Berry curvature (Fig. 7(b)), which are close to the gap closing points.

Finally, based on the TB model Eq. (D3), we discuss the quantization and physical consequence of the VCN change across the $\lambda_2 = 0$ gap closing. Without loss of generality, we take the valley in the $k_{x,y} > 0$ quarter of 1BZ as an example to discuss the quantization. The VCN of this valley can be calculated by integrating the Berry curvature over the $k_{x,y} > 0$ quarter of 1BZ. As shown in Fig. 7(c), although VCN is not quantized on any side of the gap closing, the change of VCN across the gap closing is an integer, consistent with the effective-model analysis in the main text. According to Ref. (46), one physical consequence of the quantized VCN change is the gapless domain-wall mode in a domain wall structure that consists of the two different gapped phases separated by the gap closing, like Fig. 7(d). As shown in Fig. 7(e), the VCN change for each valley matches the number of gapless domain-wall modes around that valley.

Appendix E: (111) HgTe/CdTe Quantum Well

In this section, we provide more details on the analysis of the HgTe QW. Before going into details, we first introduce some basic properties of the QW. Both HgTe and CdTe have the standard zinc-blende structure, similar to most II-VI or III-V compound semiconductors. The crystallographic space group of both compounds is $F\bar{4}3m$ (space group No. 216). In the QW, HgTe serves as a well while $\text{Hg}_{1-x}\text{Cd}_x\text{Te}$ serves as the barrier. Similar to early experimental and theoretical studies (6, 47–50), we use $x = 0.7$.

1. d -induced PET jump for $\mathcal{E} = 0$

To describe the TPQT, we project the 6-band Kane model onto the bases $(|E_1, +\rangle, |H_1, +\rangle, |E_1, -\rangle, |H_1, -\rangle)$ via second order perturbation (49) and get the following 4-band model

$$h_{eff}^{(0)}(\mathcal{E} = 0) = E_0 + B_0 k_{||}^2 + \begin{pmatrix} Bk_{||}^2 + m & A_1 k_+ & 0 & -iA_2 k_+ \\ A_1 k_- & -Bk_{||}^2 - m & -iA_2 k_+ & 0 \\ 0 & iA_2 k_- & Bk_{||}^2 + m & -A_1 k_- \\ iA_2 k_- & 0 & -A_1 k_+ & -Bk_{||}^2 - m \end{pmatrix}, \quad (\text{E1})$$

where the values of the parameters are listed Tab. 4, $k_{||}^2 = k_1^2 + k_2^2$, $k_{\pm} = k_1 \pm ik_2$, and k_1 and k_2 are the momenta along $(1, -1, 0)$ and $(1, 1, -2)$, respectively. Compared to the celebrated Bernevig-Hughes-Zhang model (6), we have an additional k -linear term A_2 due to the reduction of the full rotational symmetry to C_3 rotation symmetry. In the Eq. (E1), the TQPT shown in Fig. 2 (a) of the main text occurs at $m = 0$. To show the jump of the symmetry-allowed PET components at the gap closing, we need to introduce the electron-strain coupling $h_{eff}^{(1)}$ based on the symmetry:

$$h_{eff}^{(1)} = \xi_1 u^2 + \begin{pmatrix} \xi_2 u^2 & \xi_3 u_- & 0 & -i\xi_4 u_- \\ \xi_3 u_+ & -\xi_2 u^2 & i\xi_4 u_- & 0 \\ 0 & -i\xi_4 u_+ & \xi_2 u^2 & \xi_3 u_+ \\ i\xi_4 u_+ & 0 & \xi_3 u_- & -\xi_2 u^2 \end{pmatrix}, \quad (\text{E2})$$

where $u^2 = u_{11} + u_{22}$ and $u_{\pm} = u_{11} - u_{22} \pm i(u_{12} + u_{21})$. This electron-strain coupling is in the most general symmetry-allowed form to the leading order of u_{ij} , which definitely includes the IB terms, ξ_3 and ξ_4 . With Eq. (E1) and Eq. (E2), the independent PET component γ_{222} can be derived analytically as

$$\gamma_{222} = -e \frac{\text{sgn}(m)(A_1 \xi_3 + A_2 \xi_4)}{2\pi(A_1^2 + A_2^2)} \frac{(A_1^2 + A_2^2 - 2|Bm| + 2Bm)}{(A_1^2 + A_2^2 + 4Bm)}, \quad (\text{E3})$$

resulting in the PET jump as

$$\Delta\gamma_{222} = -e \frac{A_1\xi_3 + A_2\xi_4}{\pi(A_1^2 + A_2^2)}. \quad (\text{E4})$$

Based on Eq. (E3) and $\xi_{1,2,3,4} = 1\text{eV}$ (comparable to those in Ref. (25)), we plot the γ_{222} of the function of the width in Fig. 2 (b) of the main text, which shows a jump around $d = 65\text{\AA}$.

2. \mathcal{E} -induced PET jump for fixed d

After including the electric field, we project the modified Kane model onto the bases ($|E_1, +\rangle, |H_1, +\rangle, |E_1, -\rangle, |H_1, -\rangle$) via second order perturbation and get the following 4-band model

$$h_{eff}^{(0)} = E_0 + B_0 k_{||}^2 + \begin{pmatrix} Bk_{||}^2 + m & A_1 k_+ + D_1 k_-^2 & -iD_3 k_- & -iA_2 k_+ - iD_2 k_-^2 \\ A_1 k_- + D_1 k_+^2 & -Bk_{||}^2 - m & -iA_2 k_+ + iD_2 k_-^2 & 0 \\ iD_3 k_+ & iA_2 k_- - iD_2 k_+^2 & Bk_{||}^2 + m & D_1 k_+^2 - A_1 k_- \\ iA_2 k_- + iD_2 k_+^2 & 0 & D_1 k_-^2 - A_1 k_+ & -Bk_{||}^2 - m \end{pmatrix}. \quad (\text{E5})$$

Compared with Eq. (E1), the above Hamiltonian has three extra IB terms $D_{1,2,3}$ brought by the electric field. In fact, it is now in the most general symmetry-allowed form up to the second order of the momentum for the HgTe/CdTe QW along the (111) direction. In addition, the parameter m (mass term) can also be controlled by electric field. In the contrast to (001) QW, the constant (k -independent) IB terms in Ref. (47) are forbidden in Eq. (E5) by the C_3 symmetry. The \mathcal{E} dependence of the parameters are shown in Tab. 5 for $d = 62\text{\AA}$. Since Eq. (E2) is in the most general form, the electron-strain coupling for $\mathcal{E} \neq 0$ still keeps the form of Eq. (E2). With Eq. (E5), Eq. (E2), the parameter expression, and $\xi_{1,2,3,4} = 1\text{eV}$ comparable as those in Ref. (25), the PET jump can be calculated.

3. Projection of the Kane Model

With bases ($|\Gamma_6, \frac{1}{2}\rangle, |\Gamma_6, -\frac{1}{2}\rangle, |\Gamma_8, \frac{3}{2}\rangle, |\Gamma_8, \frac{1}{2}\rangle, |\Gamma_8, -\frac{1}{2}\rangle, |\Gamma_8, -\frac{3}{2}\rangle$), the 6-band Kane model that we use for the (111) quantum well without the electric field reads

$$h_{Kane}(\mathbf{k}) = \begin{pmatrix} h_{\Gamma_6}(\mathbf{k}) & T(\mathbf{k}) \\ T^\dagger(\mathbf{k}) & h_{\Gamma_8}(\mathbf{k}) \end{pmatrix}, \quad (\text{E6})$$

where $\mathbf{k} = (k_1, k_2, k_3)$ with $k_3 = -i\partial_{x_3}$, $h_{\Gamma_6}(\mathbf{k}) = \left(E_c + \frac{\hbar^2}{2m_0} [(2F+1)(k_1^2 + k_2^2) + k_3(2F+1)k_3]\right) \sigma_0$,

$$T(\mathbf{k}) = \begin{pmatrix} -\frac{1}{\sqrt{2}}k_+P & \sqrt{\frac{2}{3}}k_3P & \frac{1}{\sqrt{6}}k_-P & 0 \\ 0 & -\frac{1}{\sqrt{6}}k_+P & \sqrt{\frac{2}{3}}k_3P & \frac{1}{\sqrt{2}}k_-P \end{pmatrix}, \quad (\text{E7})$$

$$h_{\Gamma_8}(\mathbf{k}) = \begin{pmatrix} U+V & W & \widetilde{W} & 0 \\ W^\dagger & U-V & 0 & \widetilde{W} \\ \widetilde{W}^\dagger & 0 & U-V & -W \\ 0 & \widetilde{W}^\dagger & -W^\dagger & U+V \end{pmatrix}, \quad (\text{E8})$$

$U = E_v - \frac{\hbar^2}{2m_0} [(k_1^2 + k_2^2)\gamma_1 + k_3\gamma_1k_3]$, $V = \frac{\hbar^2}{2m_0} [-(k_1^2 + k_2^2)\gamma_3 + 2k_3\gamma_3k_3]$, $W = \frac{1}{\sqrt{3}} \frac{\hbar^2}{2m_0} [-i\sqrt{2}k_+^2(\gamma_2 - \gamma_3) + k_- \{k_3, 2\gamma_2 + \gamma_3\}]$, $\widetilde{W} = \frac{1}{\sqrt{3}} \frac{\hbar^2}{2m_0} [k_-^2(\gamma_2 + 2\gamma_3) - i\sqrt{2}k_+ \{k_3, \gamma_2 - \gamma_3\}]$, m_0 is the mass of the electron, and the IB effect is neglected. The electric field can be included by adding

$$V_e = -e\mathcal{E}x_3\mathbb{1}_6 \quad (\text{E9})$$

E_v^A	E_c^A	F^A	γ_1^A	γ_2^A	γ_3^A	P
0	-0.303	0	4.1	0.5	1.3	8.47
E_v^B	E_c^B	F^B	γ_1^B	γ_2^B	γ_3^B	
-0.399	0.607	-0.063	2.26	-0.046	0.411	

Table 3: Values of parameters in Eq. (E6) for $\text{Hg}_{0.3}\text{Cd}_{0.7}\text{Te}/\text{HgTe}/\text{Hg}_{0.3}\text{Cd}_{0.7}\text{Te}$ quantum well. The unites of E_v, E_c are eV, the unit of P is eVÅ, and other parameters are dimensionless (50, 73).

$d/\text{\AA}$	m_0/eV	$B_0/(\text{eV \AA}^2)$	m/eV	$B/(\text{eV \AA}^2)$	$A_1/(\text{eV \AA})$	$A_2/(\text{eV \AA})$
60.00	-0.006700	39.88	0.005600	60.45	3.595	0.1248
61.00	-0.007570	40.90	0.004370	61.46	3.582	0.1237
62.00	-0.008400	41.94	0.003200	62.51	3.569	0.1225
63.00	-0.009240	42.99	0.002040	63.56	3.555	0.1214
64.00	-0.01009	44.08	0.0008850	64.65	3.540	0.1204
65.00	-0.01084	45.14	-0.0001650	65.71	3.527	0.1193
66.00	-0.01159	46.25	-0.001210	66.82	3.514	0.1182
67.00	-0.01235	47.41	-0.002250	67.98	3.500	0.1172
68.00	-0.01307	48.54	-0.003230	69.12	3.486	0.1162
69.00	-0.01374	49.75	-0.004160	70.33	3.473	0.1152
70.00	-0.01442	50.98	-0.005080	71.56	3.459	0.1143

Table 4: Parameter values for Eq. (E1) at various widths d .

to Eq. (E6).

Due to the spatial dependence of the parameters, we require the anti-commutation form of some k_3 -dependent terms, such as $\{k_3, \gamma_2\}$, to keep the Hamiltonian hermitian (72). The quantum well considered has the structure $\text{Hg}_{0.3}\text{Cd}_{0.7}\text{Te}/\text{HgTe}/\text{Hg}_{0.3}\text{Cd}_{0.7}\text{Te}$, leading to the x_3 dependence of parameters $X = E_{v,c}, F, \gamma_{1,2,3}$ as

$$X = \begin{cases} X^A, & |x_3| < \frac{d}{2} \\ X^B, & |x_3| > \frac{d}{2} \end{cases}. \quad (\text{E10})$$

The numerical values of the parameters in Eq. (E6) are listed in Tab. 3.

The effective models are derived according to Ref. (6 and 49). We first numerically obtain the wavefunctions of E1, H1, LH1, HH2, and HH3 bands at $k_1 = k_2 = \mathcal{E} = 0$, and project the remaining terms to the bases to get a 10×10 Hamiltonian. Then, we project the 10×10 Hamiltonian to the E1 and H1 bands with second order perturbation to get Eq. (E1) and Eq. (E5). Keeping terms up to k^2 and \mathcal{E}^2 order, the values of the parameters are listed in Tab. 4 and Tab. 5.

4. Construction of the Hamiltonian based on symmetry

As discussed in the main text, the symmetry group of interest is generated by the three-fold rotation C_3 along (111), and the mirror $m_{1\bar{1}0}$ perpendicular to $(1, \bar{1}, 0)$ and the TR operation \mathcal{T} . With the bases $(|E_1, +\rangle, |H_1, +\rangle, |E_1, -\rangle, |H_1, -\rangle)$,

m_0/eV	$B_0/(\text{eV } \text{\AA}^2)$	m/eV
4182 $(-e\mathcal{E}/(\text{eV}\text{\AA}^{-1}))^2 - 0.008400$	544800 $(-e\mathcal{E}/(\text{eV}\text{\AA}^{-1}))^2 + 41.94$	0.003200 -17.21 $(-e\mathcal{E}/(\text{eV}\text{\AA}^{-1}))^2$
$B/(\text{eV } \text{\AA}^2)$	$A_1/(\text{eV } \text{\AA})$	$A_2/(\text{eV } \text{\AA})$
534600 $(-e\mathcal{E}/(\text{eV}\text{\AA}^{-1}))^2 + 62.51$	67320 $(-e\mathcal{E}/(\text{eV}\text{\AA}^{-1}))^2 + 3.569$	293.0 $(-e\mathcal{E}/(\text{eV}\text{\AA}^{-1}))^2 + 0.1225$
$D_1/(\text{eV } \text{\AA}^2)$	$D_2/(\text{eV } \text{\AA}^2)$	$D_3/(\text{eV } \text{\AA})$
724.7 $(-e\mathcal{E}/(\text{eV}\text{\AA}^{-1}))$	-1947 $(-e\mathcal{E}/(\text{eV}\text{\AA}^{-1}))$	-1196 $(-e\mathcal{E}/(\text{eV}\text{\AA}^{-1}))$

Table 5: Parameter values for Eq. (E5) for $d = 62\text{\AA}$.

IR	Expressions
$A_1, +$	$\sigma_0\tau_0, \sigma_0\tau_z, k_1^2 + k_2^2, u_{11} + u_{22}$
$A_1, -$	$\sigma_x\tau_-$
$A_2, +$	
$A_2, -$	$\sigma_y\tau_-, \sigma_z\tau_0, \sigma_z\tau_z$
$E, +$	$(\sigma_z\tau_y, \sigma_0\tau_x), (\sigma_y\tau_y, \sigma_x\tau_y), (2k_1k_2, k_1^2 - k_2^2), (u_{12} + u_{21}, u_{11} - u_{22})$
$E, -$	$(\sigma_z\tau_x, -\sigma_0\tau_y), (\sigma_y\tau_x, \sigma_x\tau_x), (\sigma_y\tau_+, -\sigma_x\tau_+), (k_1, k_2)$

Table 6: The irreducible representations (IRs) of C_{3v} and TR symmetries. A_1, A_2 and E are IRs of C_{3v} and \pm are parity under TR. $\tau_{\pm} = (\tau_0 \pm \tau_z)/2$.

those symmetry operations, according to the convention in Ref. (72), are represented as

$$\begin{aligned}
C_3 &\doteq \begin{pmatrix} e^{-\frac{i\pi}{3}} & 0 & 0 & 0 \\ 0 & -1 & 0 & 0 \\ 0 & 0 & e^{\frac{i\pi}{3}} & 0 \\ 0 & 0 & 0 & -1 \end{pmatrix} \\
m_{1\bar{1}0} &\doteq -i\sigma_x\tau_0 = \begin{pmatrix} 0 & 0 & -i & 0 \\ 0 & 0 & 0 & -i \\ -i & 0 & 0 & 0 \\ 0 & -i & 0 & 0 \end{pmatrix} \\
\mathcal{T} &\doteq -i\sigma_y\tau_0 = \begin{pmatrix} 0 & 0 & -1 & 0 \\ 0 & 0 & 0 & -1 \\ 1 & 0 & 0 & 0 \\ 0 & 1 & 0 & 0 \end{pmatrix} \mathcal{K},
\end{aligned} \tag{E11}$$

where τ 's and σ 's are Pauli matrices for E_1, H_1 indexes and \pm indexes, respectively. According to the symmetry representations, the matrix and momenta of the effective model can be classified as Tab. 6.

From Tab. 6, the most general symmetry-allowed Hamiltonian without the electron-strain coupling can be derived to the k^2 order, resulting in Eq. (E5). As shown in Tab. 6, u_{ij} behaves the same as the k^2 term, and thereby the electron-strain coupling has the same form as the k^2 term in Eq. (E5).

Appendix F: BaMnSb₂

In this section, we include more details on BaMnSb₂.

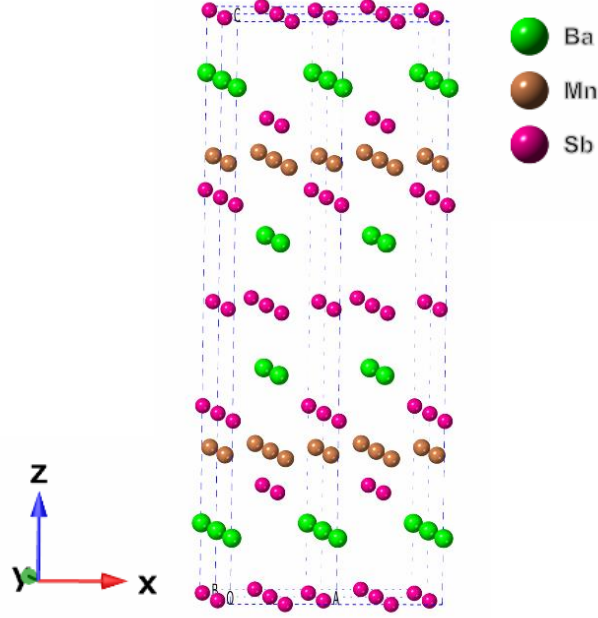


Fig 8: The crystalline structure of BaMnSb₂ generated from CrystalMaker.

1. Review

In this part, we review the form and the dispersion of the TB model derived in Ref. (52) for integrity. This part does not contain any original results. More details can be found in Ref. (52).

According to the main text, there are two Sb atoms in one unit cell, labeled as 1 and 2, that have sub-lattice vectors $\tau_1 = (x_1 a, 0)$ and $\tau_2 = (x_2 a, b/2)$, respectively. a, b are the lattice constants of the unit cell in x, y direction and the values of $x_{1,2}$ are given later. Combined with p_x and p_y orbitals, the bases of the TB model are $|\mathbf{R} + \tau_i, \alpha, s\rangle$ with the lattice vector $\mathbf{R} = (l_x a, l_y b)$ ($l_{x,y} \in \mathbb{Z}$), the sublattice index $i = 1, 2$, the orbital index $\alpha = p_x, p_y$, and the spin- z index $s = \uparrow, \downarrow$. The TB model consists of the on-site term H_0 , the nearest-neighboring (NN) hopping H_1 and the next-NN hopping H_2 in the TB model, *i.e.* $H_{TB} = H_0 + H_1 + H_2$. H_0 has the form

$$H_0 = \sum_{\mathbf{R}, i} c_{\mathbf{R} + \tau_i}^\dagger M_i c_{\mathbf{R} + \tau_i} \quad (\text{F1})$$

with

$$c_{\mathbf{R} + \tau_i}^\dagger = (c_{\mathbf{R} + \tau_i, p_x, \uparrow}^\dagger, c_{\mathbf{R} + \tau_i, p_x, \downarrow}^\dagger, c_{\mathbf{R} + \tau_i, p_y, \uparrow}^\dagger, c_{\mathbf{R} + \tau_i, p_y, \downarrow}^\dagger) . \quad (\text{F2})$$

H_1 reads

$$H_1 = \sum_{\mathbf{R}} \sum_{n=1}^4 c_{\mathbf{R} + \Delta \mathbf{R}_n + \tau_2}^\dagger T_n c_{\mathbf{R} + \tau_1} + h.c. , \quad (\text{F3})$$

where $\Delta \mathbf{R}_1 = (0, 0)$, $\Delta \mathbf{R}_2 = (a, 0)$, $\Delta \mathbf{R}_3 = (a, -b)$ and $\Delta \mathbf{R}_4 = (0, -b)$. H_2 reads

$$H_2 = \sum_{\mathbf{R}, i} \sum_{n=x, y} c_{\mathbf{R} + \Delta \mathbf{R}_n + \tau_i}^\dagger Q_{ni} c_{\mathbf{R} + \tau_i} + h.c. , \quad (\text{F4})$$

where $\Delta \mathbf{R}_x = (a, 0)$ and $\Delta \mathbf{R}_y = (0, b)$. The forms of M 's, T 's, and Q 's are

$$\begin{aligned}
M_1 &= \tilde{m}_0 \tau_0 \sigma_0 + \tilde{m}_1 \tau_z \sigma_0 + \lambda_0 \tau_y \sigma_z , \\
M_2 &= C_{4z}^{OS} M_1 (C_{4z}^{OS})^\dagger , \\
T_1 &= t_0 \tau_0 \sigma_0 + t_1 \tau_x \sigma_0 + i t_2 \tau_y \sigma , T_2 = \frac{\tau_z \sigma_y T_1 \tau_z \sigma_y}{f(\alpha)} , \\
T_4 &= \tau_z \sigma_y T_1 \tau_z \sigma_y , T_3 = \frac{T_1}{f(\alpha)} , \\
Q_{x1} &= t_3 \tau_0 \sigma_0 + t_4 \tau_z \sigma_0 , Q_{x2} = t_5 \tau_0 \sigma_0 + t_6 \tau_z \sigma_0 , \\
Q_{y1} &= C_{4z}^{OS} Q_{x2} (C_{4z}^{OS})^\dagger , Q_{y2} = C_{4z}^{OS} Q_{x1} (C_{4z}^{OS})^\dagger ,
\end{aligned} \tag{F5}$$

where $f(\alpha) = 0.2\alpha + 1$, and $C_{4z}^{OS} = (-i\tau_y)e^{-i\frac{\sigma_z}{2}\frac{\pi}{2}}$ is the representation of the four-fold rotation along z in the orbital and spin subspace. α is the dimensionless distortion parameter; $\alpha = 0$ and $\alpha = 1$ correspond to the non-distorted and fully distorted cases, respectively. Moreover, the distortion effect on the relative atom positions is chosen as $x_1 = \frac{1}{2} + (0.4512 - \frac{1}{2})\alpha$ and $x_2 = 0.01729\alpha$, while we neglect distortion-induced change of a and b .

The numerical calculation is done for

$$\begin{aligned}
\tilde{m}_0 &= 0 , \tilde{m}_1 = 0.3\text{eV} , \lambda_0 = 0.25\text{eV} , t_0 = 1\text{eV} , \\
t_1 &= 2\text{eV} , t_2 = 0 , t_3 = 0.1\text{eV} , t_4 = -0.06\text{eV} , \\
t_5 &= 0.15\text{eV} , t_6 = -0.06\text{eV} , \text{ and } a = b = 4.5\text{\AA} .
\end{aligned} \tag{F6}$$

The energy dispersion for $\alpha = 1$ is shown in the supplementary material of Ref. (52).

2. TB Calculation of PET

The main effect of the strain in the TB model is to change the hopping amplitudes among atoms (16, 74), which can be modeled by performing the following replacement (74) to the hopping parameters:

$$t_{ab} \rightarrow \left(1 - \beta \frac{\delta_i \delta_j u_{ij}}{|\delta|^2}\right) t_{ab} \tag{F7}$$

, where t_{ab} is the hopping parameter between atoms at \mathbf{r}_a and \mathbf{r}_b in the non-deformed case, and $\delta = \mathbf{r}_a - \mathbf{r}_b$. β is the electron-phonon coupling parameter whose value for BaMnSb₂ has not been determined, and thereby we adopt the typical value $\beta = 2$ for the TMDs (74) to give a reasonable estimation of the PET jump.

3. Effective Model Analysis

To analytically demonstrate the PET jump, we project the tight-binding model into the subspace spanned by two degenerate states at each gap closing point (valley). As discussed in Ref. (52), the resultant effective model reads

$$h_{\pm}^{(0)}(\mathbf{q}) = (E_0 \pm v_0 q_y) \tau_0 \pm v_2 q_y \tau_z \pm v_1 q_x \tau_x \pm (E_1 + \lambda) \tau_y , \tag{F8}$$

where $h_{\pm}(\mathbf{q})$ is around \mathbf{K}_{\pm} with $\mathbf{q} = \mathbf{k} - \mathbf{K}_{\pm}$, the two bases of $h_{\pm}^{(0)}$ ($h_{\pm}^{(0)}$) are $|\mathbf{K}_{+}, p_x \pm i p_y, \uparrow\rangle$ ($|\mathbf{K}_{-}, p_x \pm i p_y, \downarrow\rangle$), and the term with small coefficient has been omitted. E_1 and v_1 are given by the distortion, λ labels the SOC strength, and we choose $E_1 < 0, \lambda > 0$ without loss of generality. According to Eq. (F8), the gap closing can be achieved by tuning the distortion parameter E_1 to $E_1 + \lambda = 0$, which changes the Z_2 index since only one Dirac cone appears in half 1BZ. To study the PET jump, we include the electron-strain coupling with the form

$$h_{\pm}^{(1)}(\mathbf{q}) = N_0 \tau_0 + N_1 \tau_x + N_2 \tau_z , \tag{F9}$$

where $N_1 = \xi_{xy}(u_{xy} + u_{yx})$ and $N_i = \xi_{i,xx}u_{xx} + \xi_{i,yy}u_{yy}$ for $i = 0, 2$. It is derived from the symmetry consideration and the fact that the τ_y term is valley-dependent and thus of higher order. Combining the above equation with Eq. (F8),

we obtain the non-zero PET jump

$$\begin{aligned}\Delta\gamma_{xxx} &= -e \frac{\text{sgn}(v_1 v_2)}{\pi v_2} \xi_{2,xx} \\ \Delta\gamma_{xyy} &= -e \frac{\text{sgn}(v_1 v_2)}{\pi v_2} \xi_{2,yy} \\ \Delta\gamma_{xyx} &= \Delta\gamma_{yyx} = e \frac{\text{sgn}(v_1 v_2)}{\pi v_1} \xi_{xy} ,\end{aligned}\tag{F10}$$

as E_1 is tuned from $-\lambda + 0^-$ to $-\lambda + 0^+$. Therefore, the gap closing and the PET jump are consistent with result for scenario (iii) of $p1m1$.

-
- [1] Xiao-Liang Qi and Shou-Cheng Zhang, “Topological insulators and superconductors,” *Rev. Mod. Phys.* **83**, 1057–1110 (2011).
 - [2] M. Z. Hasan and C. L. Kane, “Colloquium: Topological insulators,” *Rev. Mod. Phys.* **82**, 3045–3067 (2010).
 - [3] Ching-Kai Chiu, Jeffrey C. Y. Teo, Andreas P. Schnyder, and Shinsei Ryu, “Classification of topological quantum matter with symmetries,” *Rev. Mod. Phys.* **88**, 035005 (2016).
 - [4] Bodo Huckestein, “Scaling theory of the integer quantum hall effect,” *Rev. Mod. Phys.* **67**, 357–396 (1995).
 - [5] D. J. Thouless, M. Kohmoto, M. P. Nightingale, and M. den Nijs, “Quantized hall conductance in a two-dimensional periodic potential,” *Phys. Rev. Lett.* **49**, 405–408 (1982).
 - [6] B. Andrei Bernevig, Taylor L. Hughes, and Shou-Cheng Zhang, “Quantum spin hall effect and topological phase transition in hgte quantum wells,” *Science* **314**, 1757–1761 (2006).
 - [7] Xiao-Liang Qi, Taylor L. Hughes, and Shou-Cheng Zhang, “Topological field theory of time-reversal invariant insulators,” *Phys. Rev. B* **78**, 195424 (2008).
 - [8] Masataka Mogi, Minoru Kawamura, Atsushi Tsukazaki, Ryutaro Yoshimi, Kei S. Takahashi, Masashi Kawasaki, and Yoshinori Tokura, “Tailoring tricolor structure of magnetic topological insulator for robust axion insulator,” *Science Advances* **3** (2017), 10.1126/sciadv.aao1669.
 - [9] Di Xiao, Jue Jiang, Jae-Ho Shin, Wenbo Wang, Fei Wang, Yi-Fan Zhao, Chaoxing Liu, Weida Wu, Moses H. W. Chan, Nitin Samarth, and Cui-Zu Chang, “Realization of the axion insulator state in quantum anomalous hall sandwich heterostructures,” *Phys. Rev. Lett.* **120**, 056801 (2018).
 - [10] Jiabin Yu, Jiadong Zang, and Chao-Xing Liu, “Magnetic resonance induced pseudoelectric field and giant current response in axion insulators,” *Phys. Rev. B* **100**, 075303 (2019).
 - [11] Richard M. Martin, “Piezoelectricity,” *Phys. Rev. B* **5**, 1607–1613 (1972).
 - [12] David Vanderbilt and R. D. King-Smith, “Electric polarization as a bulk quantity and its relation to surface charge,” *Phys. Rev. B* **48**, 4442–4455 (1993).
 - [13] R. D. King-Smith and David Vanderbilt, “Theory of polarization of crystalline solids,” *Phys. Rev. B* **47**, 1651–1654 (1993).
 - [14] Raffaele Resta and David Vanderbilt, “Theory of polarization: A modern approach,” in *Physics of Ferroelectrics: A Modern Perspective* (Springer Berlin Heidelberg, Berlin, Heidelberg, 2007) pp. 31–68.
 - [15] D Vanderbilt, “Berry-phase theory of proper piezoelectric response,” *Journal of Physics and Chemistry of Solids* **61**, 147–151 (2000).
 - [16] Yunhua Wang, Zongtan Wang, Jie Li, Jie Tan, Biao Wang, and Yulan Liu, “Tight-binding piezoelectric theory and electromechanical coupling correlations for transition metal dichalcogenide monolayers,” *Phys. Rev. B* **98**, 125402 (2018).
 - [17] R. L. E. Schwarzenberger, “The 17 plane symmetry groups,” *The Mathematical Gazette* **58**, 123–131 (1974).
 - [18] Theo Hahn, Uri Shmueli, and JC Wilson Arthur, *International tables for crystallography*, Vol. 1 (Reidel Dordrecht, 1983).
 - [19] Andrei L Kholkin, Nikolay A Pertsev, and Alexander V Goltsev, “Piezoelectricity and crystal symmetry,” in *Piezoelectric and Acoustic Materials for Transducer Applications* (Springer, 2008) pp. 17–38.
 - [20] Fan Zhang, Allan H MacDonald, and Eugene J Mele, “Valley chern numbers and boundary modes in gapped bilayer graphene,” *Proceedings of the National Academy of Sciences* **110**, 10546–10551 (2013).
 - [21] Chen Fang and Liang Fu, “New classes of three-dimensional topological crystalline insulators: Nonsymmorphic and magnetic,” *Phys. Rev. B* **91**, 161105 (2015).
 - [22] M.A.H. Vozmediano, M.I. Katsnelson, and F. Guinea, “Gauge fields in graphene,” *Physics Reports* **496**, 109–148 (2010).
 - [23] Abolhassan Vaezi, Nima Abedpour, Reza Asgari, Alberto Cortijo, and María A. H. Vozmediano, “Topological electric current from time-dependent elastic deformations in graphene,” *Phys. Rev. B* **88**, 125406 (2013).
 - [24] Matthias Droth, Guido Burkard, and Vitor M. Pereira, “Piezoelectricity in planar boron nitride via a geometric phase,” *Phys. Rev. B* **94**, 075404 (2016).
 - [25] Habib Rostami, Francisco Guinea, Marco Polini, and Rafael Roldán, “Piezoelectricity and valley chern number in inhomogeneous hexagonal 2d crystals,” *npj 2D Materials and Applications* **2**, 15 (2018).
 - [26] Shuichi Murakami, Satoshi Iso, Yshai Avishai, Masaru Onoda, and Naoto Nagaosa, “Tuning phase transition between quantum spin hall and ordinary insulating phases,” *Phys. Rev. B* **76**, 205304 (2007).

- [27] J. E. Moore and L. Balents, “Topological invariants of time-reversal-invariant band structures,” *Phys. Rev. B* **75**, 121306 (2007).
- [28] Hidekatsu Suzuura and Tsuneya Ando, “Phonons and electron-phonon scattering in carbon nanotubes,” *Phys. Rev. B* **65**, 235412 (2002).
- [29] Francisco Guinea, MI Katsnelson, and AK Geim, “Energy gaps and a zero-field quantum hall effect in graphene by strain engineering,” *Nature Physics* **6**, 30 (2010).
- [30] Barry Bradlyn, L Elcoro, Jennifer Cano, MG Vergniory, Zhijun Wang, C Felser, MI Aroyo, and B Andrei Bernevig, “Topological quantum chemistry,” *Nature* **547**, 298 (2017).
- [31] Barry Bradlyn, L. Elcoro, M. G. Vergniory, Jennifer Cano, Zhijun Wang, C. Felser, M. I. Aroyo, and B. Andrei Bernevig, “Band connectivity for topological quantum chemistry: Band structures as a graph theory problem,” *Phys. Rev. B* **97**, 035138 (2018).
- [32] Jennifer Cano, Barry Bradlyn, Zhijun Wang, L. Elcoro, M. G. Vergniory, C. Felser, M. I. Aroyo, and B. Andrei Bernevig, “Building blocks of topological quantum chemistry: Elementary band representations,” *Phys. Rev. B* **97**, 035139 (2018).
- [33] Jennifer Cano, Barry Bradlyn, Zhijun Wang, L. Elcoro, M. G. Vergniory, C. Felser, M. I. Aroyo, and B. Andrei Bernevig, “Topology of disconnected elementary band representations,” *Phys. Rev. Lett.* **120**, 266401 (2018).
- [34] Barry Bradlyn, Zhijun Wang, Jennifer Cano, and B. Andrei Bernevig, “Disconnected elementary band representations, fragile topology, and wilson loops as topological indices: An example on the triangular lattice,” *Phys. Rev. B* **99**, 045140 (2019).
- [35] Benjamin J Wieder and B Andrei Bernevig, “The axion insulator as a pump of fragile topology,” [arXiv:1810.02373](https://arxiv.org/abs/1810.02373) (2018).
- [36] Benjamin J. Wieder, Zhijun Wang, Jennifer Cano, Xi Dai, Leslie M. Schoop, Barry Bradlyn, and B. Andrei Bernevig, “Strong and fragile topological dirac semimetals with higher-order fermi arcs,” *Nature Communications* **11**, 627 (2020).
- [37] Hoi Chun Po, Ashvin Vishwanath, and Haruki Watanabe, “Symmetry-based indicators of band topology in the 230 space groups,” *Nature communications* **8**, 50 (2017).
- [38] Jorrit Kruthoff, Jan de Boer, Jasper van Wezel, Charles L. Kane, and Robert-Jan Slager, “Topological classification of crystalline insulators through band structure combinatorics,” *Phys. Rev. X* **7**, 041069 (2017).
- [39] Haruki Watanabe, Hoi Chun Po, and Ashvin Vishwanath, “Structure and topology of band structures in the 1651 magnetic space groups,” *Science Advances* **4** (2018), 10.1126/sciadv.aat8685.
- [40] Zhida Song, Tiantian Zhang, Zhong Fang, and Chen Fang, “Quantitative mappings between symmetry and topology in solids,” *Nature Communications* **9**, 3530 (2018).
- [41] Xiao-Yu Dong and Chao-Xing Liu, “Classification of topological crystalline insulators based on representation theory,” *Phys. Rev. B* **93**, 045429 (2016).
- [42] Ching-Kai Chiu, Hong Yao, and Shinsei Ryu, “Classification of topological insulators and superconductors in the presence of reflection symmetry,” *Phys. Rev. B* **88**, 075142 (2013).
- [43] Ken Shiozaki and Masatoshi Sato, “Topology of crystalline insulators and superconductors,” *Phys. Rev. B* **90**, 165114 (2014).
- [44] Junyeong Ahn and Bohm-Jung Yang, “Unconventional topological phase transition in two-dimensional systems with space-time inversion symmetry,” *Phys. Rev. Lett.* **118**, 156401 (2017).
- [45] Sungjoon Park and Bohm-Jung Yang, “Classification of accidental band crossings and emergent semimetals in two-dimensional noncentrosymmetric systems,” *Phys. Rev. B* **96**, 125127 (2017).
- [46] Jian Li, Alberto F. Morpurgo, Markus Büttiker, and Ivar Martin, “Marginality of bulk-edge correspondence for single-valley hamiltonians,” *Phys. Rev. B* **82**, 245404 (2010).
- [47] Markus König, Steffen Wiedmann, Christoph Brüne, Andreas Roth, Hartmut Buhmann, Laurens W. Molenkamp, Xiao-Liang Qi, and Shou-Cheng Zhang, “Quantum spin hall insulator state in hgte quantum wells,” *Science* **318**, 766–770 (2007).
- [48] Jun Li and Kai Chang, “Electric field driven quantum phase transition between band insulator and topological insulator,” *Applied Physics Letters* **95**, 222110 (2009).
- [49] D G Rothe, R W Reinthaler, C-X Liu, L W Molenkamp, S-C Zhang, and E M Hankiewicz, “Fingerprint of different spin-orbit terms for spin transport in HgTe quantum wells,” *New Journal of Physics* **12**, 065012 (2010).
- [50] E. G. Novik, A. Pfeuffer-Jeschke, T. Jungwirth, V. Latussek, C. R. Becker, G. Landwehr, H. Buhmann, and L. W. Molenkamp, “Band structure of semimagnetic $\text{Hg}_{1-y}\text{Mn}_y\text{Te}$ quantum wells,” *Phys. Rev. B* **72**, 035321 (2005).
- [51] Hanyu Zhu, Yuan Wang, Jun Xiao, Ming Liu, Shaomin Xiong, Zi Jing Wong, Ziliang Ye, Yu Ye, Xiaobo Yin, and Xiang Zhang, “Observation of piezoelectricity in free-standing monolayer MoS_2 ,” *Nature Nanotechnology* **10**, 151 EP – (2014).
- [52] JY Liu, J Yu, JL Ning, L Miao, LJ Min, KA Lopez, YL Zhu, HM Yi, T Pillsbury, YB Zhang, *et al.*, “Surface chiral metal in a bulk half-integer quantum hall insulator,” [arXiv preprint arXiv:1907.06318](https://arxiv.org/abs/1907.06318) (2019).
- [53] Liang Fu and C. L. Kane, “Time reversal polarization and a Z_2 adiabatic spin pump,” *Phys. Rev. B* **74**, 195312 (2006).
- [54] Ivan Knez, Rui-Rui Du, and Gerard Sullivan, “Evidence for helical edge modes in inverted InAs/GaSb quantum wells,” *Phys. Rev. Lett.* **107**, 136603 (2011).
- [55] Shujie Tang, Chaofan Zhang, Dillon Wong, Zahra Pedramrazi, Hsin-Zon Tsai, Chunjing Jia, Brian Moritz, Martin Claassen, Hyejin Ryu, Salman Kahn, Juan Jiang, Hao Yan, Makoto Hashimoto, Donghui Lu, Robert G. Moore, Chan-Cuk Hwang, Choongyu Hwang, Zahid Hussain, Yulin Chen, Miguel M. Ugeda, Zhi Liu, Xiaoming Xie, Thomas P. Devereaux, Michael F. Crommie, Sung-Kwan Mo, and Zhi-Xun Shen, “Quantum spin hall state in monolayer $\text{1T}'\text{-WTe}_2$,” *Nature Physics* **13**, 683 EP – (2017).
- [56] Zaiyao Fei, Tauno Palomaki, Sanfeng Wu, Wenjin Zhao, Xinghan Cai, Bosong Sun, Paul Nguyen, Joseph Finney, Xiaodong Xu, and David H. Cobden, “Edge conduction in monolayer WTe_2 ,” *Nature Physics* **13**, 677 EP – (2017).

- [57] Sanfeng Wu, Valla Fatemi, Quinn D. Gibson, Kenji Watanabe, Takashi Taniguchi, Robert J. Cava, and Pablo Jarillo-Herrero, “Observation of the quantum spin hall effect up to 100 kelvin in a monolayer crystal,” *Science* **359**, 76–79 (2018).
- [58] Xiaofeng Qian, Junwei Liu, Liang Fu, and Ju Li, “Quantum spin hall effect in two-dimensional transition metal dichalcogenides,” *Science* **346**, 1344–1347 (2014).
- [59] J. O. Island, X. Cui, C. Lewandowski, J. Y. Khoo, E. M. Spanton, H. Zhou, D. Rhodes, J. C. Hone, T. Taniguchi, K. Watanabe, L. S. Levitov, M. P. Zaletel, and A. F. Young, “Spin-orbit-driven band inversion in bilayer graphene by the van der waals proximity effect,” *Nature* **571**, 85–89 (2019).
- [60] Michael P Zaletel and Jun Yong Khoo, “The gate-tunable strong and fragile topology of multilayer-graphene on a transition metal dichalcogenide,” arXiv preprint arXiv:1901.01294 (2019).
- [61] Wenzhuo Wu, Lei Wang, Yilei Li, Fan Zhang, Long Lin, Simiao Niu, Daniel Chenet, Xian Zhang, Yufeng Hao, Tony F. Heinz, James Hone, and Zhong Lin Wang, “Piezoelectricity of single-atomic-layer mos2 for energy conversion and piezotronics,” *Nature* **514**, 470 EP – (2014).
- [62] Ruixiang Fei, Wenbin Li, Ju Li, and Li Yang, “Giant piezoelectricity of monolayer group iv monochalcogenides: Snse, sns, gese, and ges,” *Applied Physics Letters* **107**, 173104 (2015).
- [63] Sinisa Coh and David Vanderbilt, “Electric polarization in a chern insulator,” *Phys. Rev. Lett.* **102**, 107603 (2009).
- [64] Vladimir A. Benalcazar, B. Andrei Bernevig, and Taylor L. Hughes, “Quantized electric multipole insulators,” *Science* **357**, 61–66 (2017).
- [65] Frank Schindler, Ashley M. Cook, Maia G. Vergniory, Zhijun Wang, Stuart S. P. Parkin, B. Andrei Bernevig, and Titus Neupert, “Higher-order topological insulators,” *Science Advances* **4** (2018), 10.1126/sciadv.aat0346.
- [66] Zhida Song, Zhong Fang, and Chen Fang, “ $(d - 2)$ -dimensional edge states of rotation symmetry protected topological states,” *Phys. Rev. Lett.* **119**, 246402 (2017).
- [67] Josias Langbehn, Yang Peng, Luka Trifunovic, Felix von Oppen, and Piet W. Brouwer, “Reflection-symmetric second-order topological insulators and superconductors,” *Phys. Rev. Lett.* **119**, 246401 (2017).
- [68] Hoi Chun Po, Haruki Watanabe, and Ashvin Vishwanath, “Fragile topology and wannier obstructions,” *Phys. Rev. Lett.* **121**, 126402 (2018).
- [69] Dániel Varjas, Adolfo G. Grushin, Roni Ilan, and Joel E. Moore, “Dynamical piezoelectric and magnetopiezoelectric effects in polar metals from berry phases and orbital moments,” *Phys. Rev. Lett.* **117**, 257601 (2016).
- [70] Jing Li, Rui-Xing Zhang, Zhenxi Yin, Jianxiao Zhang, Kenji Watanabe, Takashi Taniguchi, Chaoxing Liu, and Jun Zhu, “A valley valve and electron beam splitter,” *Science* **362**, 1149–1152 (2018).
- [71] Liang Fu and C. L. Kane, “Topological insulators with inversion symmetry,” *Phys. Rev. B* **76**, 045302 (2007).
- [72] R Winkler, SJ Papadakis, EP De Poortere, and M Shayegan, *Spin-Orbit Coupling in Two-Dimensional Electron and Hole Systems*, Vol. 41 (Springer, 2003) pp. 211–223.
- [73] J. P. Laurenti, J. Camassel, A. Bouhemadou, B. Toulouse, R. Legros, and A. Lusson, “Temperature dependence of the fundamental absorption edge of mercury cadmium telluride,” *Journal of Applied Physics* **67**, 6454–6460 (1990).
- [74] Linhu Li, Eduardo V. Castro, and Pedro D. Sacramento, “Strain-induced topological phase transition at zigzag edges of monolayer transition-metal dichalcogenides,” *Phys. Rev. B* **94**, 195419 (2016).